NASA TECHNICAL MEMORANDUM

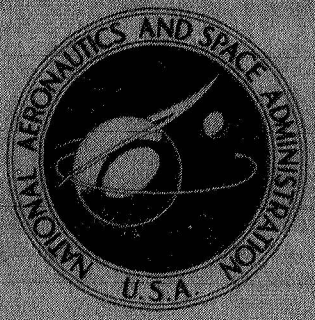

NASA TM X-3235

NASA TM X-3235

FLIGHT TRANSITION DATA FOR ANGLES OF ATTACK AT MACH 22 WITH CORRELATIONS OF THE DATA

Charles B. Johnson and Christine M. Darden

Langley Research Center
Hampton, Va. 23665

NATIONAL AERONAUTICS AND SPACE ADMINISTRATION • WASHINGTON, D. C. • AUGUST 1975

1. Report No.	2. Government Accession No.	3. Recipient's Catalog No.
NASA TM X-3235		

4. Title and Subtitle	5. Report Date
FLIGHT TRANSITION DATA FOR ANGLES OF ATTACK AT MACH 22 WITH CORRELATIONS OF THE DATA	August 1975
	6. Performing Organization Code

7. Author(s)	8. Performing Organization Report No.
Charles B. Johnson and Christine M. Darden	L-10143
	10. Work Unit No.
	505-11-31-02

9. Performing Organization Name and Address	11. Contract or Grant No.
NASA Langley Research Center Hampton, Va. 23665	
	13. Type of Report and Period Covered
12. Sponsoring Agency Name and Address	Technical Memorandum
National Aeronautics and Space Administration Washington, D.C. 20546	14. Sponsoring Agency Code

15. Supplementary Notes

16. Abstract

Boundary-layer transition data for angles of attack from 2.5° to 47° from a flight experiment with a cone that reentered at angles of attack up to 75° are analyzed and their local flow conditions presented. The transition data were obtained from both acoustic and electrostatic sensors. There are 102 transitional and turbulent data points from electrostatic sensors and 16 data points from acoustic sensors. Previously unpublished local flow properties are presented for the 93 transitional and turbulent data points and for the 139 laminar data points all from the electrostatic sensors. The data from the acoustic and electrostatic sensors are correlated by use of three different sets of correlating parameters. For each set of correlating parameters, the transitional and turbulent data from the acoustic and electrostatic sensors are plotted separately. Each of the correlations was compared with a linear curve fit of previous cone-flight data at near zero angle of attack. The data from acoustic sensors fell below the linear curve fits to the flight data and indicated the sensitivity of the sensors and also that the acoustic sensors were probably detecting the onset of transition. The transition data from the electrostatic sensors tended to scatter much more than the data from the acoustic sensors did. However, the data from the electrostatic sensors tend to scatter about the linear curve fits based on previous flight data.

17. Key Words (Suggested by Author(s))	18. Distribution Statement
Flight transition data Turbulent boundary layer Transition at angle of attack	Unclassified – Unlimited New Subject Category 34

19. Security Classif. (of this report)	20. Security Classif. (of this page)	21. No. of Pages	22. Price*
Unclassified	Unclassified	29	$3.75

*For sale by the National Technical Information Service, Springfield, Virginia 22161

FLIGHT TRANSITION DATA FOR ANGLES OF ATTACK AT MACH 22 WITH CORRELATIONS OF THE DATA

Charles B. Johnson and Christine M. Darden
Langley Research Center

SUMMARY

Boundary-layer transition data for angles of attack from 2.5° to 47° from a flight experiment with a cone that reentered at angles of attack up to 75° are analyzed and their local flow conditions presented. The transition data were obtained from both acoustic and electrostatic sensors. There are 102 transitional and turbulent data points from electrostatic sensors and 16 data points from acoustic sensors. Previously unpublished local flow properties are presented for the 93 transitional and turbulent data points and for the 139 laminar data points all from the electrostatic sensors. The data from the acoustic and electrostatic sensors are correlated by use of three different sets of correlating parameters. For each set of correlating parameters, the transitional and turbulent data from the acoustic and electrostatic sensors are plotted separately. Each of the correlations was compared with a linear curve fit of previous cone-flight data at near zero angle of attack. The data from acoustic sensors fell below the linear curve fits to the flight data and indicated the sensitivity of the sensors and also that the acoustic sensors were probably detecting the onset of transition. The transition data from the electrostatic sensors tended to scatter much more than the data from the acoustic sensors did. However, the data from the electrostatic sensors tend to scatter about the linear curve fits based on previous flight data.

INTRODUCTION

The heat protection system required for an entry vehicle or hypersonic cruise vehicle depends in part on the ability to predict the location of the onset of transition. The development of the space shuttle has focused interest on the effect of angle of attack on the location of the start and end of transition. There has been a concerted effort to develop a theoretical prediction of where transition occurs in the laminar boundary layer; however, to date the prediction of the location of the onset of transition is largely based on empirical correlations of ground test data with limited amounts of flight data (about 10 percent of the total number of transition data points, see refs. 1 and 2). Much of the known free flight, ballistic range, and ground test data (primarily for $\alpha \approx 0$) are presented

in references 1 to 3 in the form of various correlations. In recent years there has been a concerted effort to obtain transition data from ground tests on specific shuttle configurations and on simplified geometries based on generalized space shuttle shapes (see refs. 4 to 6), both types of configurations being tested over a wide range of angle of attack. However, since much of the flight data of transition given in references 1 to 3 were obtained at angles of attack of 0°, there was a need for additional flight transition data at large angles of attack for analysis of boundary-layer transition on the space shuttle.

One source of much of the flight transition data at angles of attack from approximately 2.5° to 47° was supplied from a flight experiment with a cone which was designed to reenter at a nominal angle of attack of 0°; however, because of some anomaly above the Earth's atmosphere, the cone had an oscillatory reentry with initial angles of attack up to 75°. The transition data from this anomalous flight are presented in references 7 and 8; however, the analysis of the transition data based on local flow conditions is very limited and the purpose of this paper is to present a more detailed analysis with local flow conditions calculated for laminar, transitional, and turbulent data points. In addition, this paper will present the data points by use of the most recent correlating parameters presented in reference 2.

SYMBOLS

F_2 defined by equations (4) and (7)

h static enthalpy

l nondimensionalizing constant length used in calculating unit Reynolds number (see eq. (1)), can be 1 meter, 1 foot, model length, or some other constant length

M Mach number

R local unit Reynolds number

$R_{e,x}$ local Reynolds number based on axial distance to transition

R_{e,δ^*} local transition Reynolds number based on δ^* (see eq. (2))

$\overline{R}_{e,\delta^*}$ local transition Reynolds number based on δ^*, calculated by method of reference 8

R_l	unit Reynolds number nondimensionalized by l
T	absolute temperature
u	local velocity
V	velocity of flight vehicle
x	axial distance to transition from virtual origin of vehicle
α	local angle of attack
$\alpha_{\text{¢}}$	angle of attack relative to vehicle center line
γ	ratio of specific heats
δ^*	displacement thickness
θ	momentum thickness
μ	coefficient of viscosity
Φ	azimuth angle (see fig. 1)
ρ	density
σ_x	standard deviation
ψ	angle relative to windward meridian

Subscripts:

e	local conditions at edge of boundary layer
i	incompressible
w	wall
∞	free stream ahead of body shock

FLIGHT VEHICLE AND INSTRUMENTATION

The cone and associated instrumentation which was used to obtain the flight boundary-layer transition data at angle of attack is shown in figure 1. The reentry vehicle was an 8° half-angle beryllium cone, which had a 2.54-mm-radius graphite nose, and reentered the Earth's atmosphere at approximately 6.9 km/sec at an angle of attack up to 75°.

Two flights of this particular configuration were made by a contractor for the U.S. Department of Defense. The first of these two flights (referred to as flight 1 in ref. 8) reentered at high angles of attack because of some anomaly above the Earth's atmosphere. (See fig. 2.) The second of these heavily instrumented flights entered at the design angle of attack of 0° (referred to as flight 2 in ref. 8). The transition data from flight 2 were analyzed to provide a method for the interpretation of the output of the electrostatic and acoustic sensor of the high angle-of-attack data from flight 1. However, the results of the anomalous angle-of-attack flight were of no use to the Department of Defense and were not reduced until funds were made available by the Langley Research Center.

The vehicle has a nearly constant rolling motion of approximately 15 revolutions per minute in addition to the pitching motion shown in figure 2. As a result of these motions, the various rays of instrumentation are at some instant on the windward meridian. The motion of the vehicle caused a rapid change in the local angle of attack which coupled with the rapid change in free-stream conditions resulted in a large variation of flow properties at the edge of the boundary layer. This body motion further caused a particular sensor, for the instances when it was on the windward meridian, to indicate a turbulent, then laminar, and then turbulent boundary layer for high, then low, and then high local angles of attack, respectively. Later analysis showed that an indication of the type of boundary could also be found when the sensor was far away from the windward meridian.

RESULTS AND DISCUSSION

In the initial phase of the analysis of the data from the high-angle-of-attack flight (flight 1), only the transition data obtained from acoustic sensors were used to determine whether the boundary layer was laminar, transitional, or turbulent. The transitional data for the acoustic sensors are presented in table I and include the free-stream Mach number, the vehicle center-line angle of attack, the location of the sensor, the type of boundary layer at the sensor, the local Mach number, the local flow angle, and the local Reynolds number based on (1) axial distance to the sensor, (2) local momentum thickness,

and (3) local displacement thickness. The flow-field and boundary-layer properties presented in all tables (tables I to IV) were calculated by using the small-cross-flow theory presented in reference 8. The assumption of a relatively sharp nose cone was used in the calculation; its use seemed to be justified because the first sensors were approximately 327 nose radii downstream from the nose. In addition, any possible changes in the nose shape due to ablation during reentry were neglected in the calculation. Eight of the transition data points were obtained when the acoustic sensor was on the windward meridian ($\psi = 0$); and nine of the data points indicating a turbulent boundary layer were obtained from the acoustic sensor when it was off the windward meridian. These data from the acoustic sensor were first presented in reference 6 in both tabular form and in three different boundary-layer transition correlations applicable to the space-shuttle transition criterion. The boundary-layer transition data from the acoustic sensors are also presented in reference 8 with about the same tabular listing of the local flow properties as those given in table I.

At the time that the study of the transition data from the acoustic sensors was nearly completed, it was determined that much more transition data could be obtained from the eight electrostatic sensors on the same flight vehicle. (See fig. 1.) The electrostatic sensors indicate the onset of transition when a fluctuation of the charged particles in the boundary layer is detected. For a further explanation of the techniques used for obtaining transition data from both the acoustic and electrostatic sensors, see reference 8. Initially, the data from the electrostatic sensors were obtained by examining the output from the sensors when they were on the windward meridian ($\psi = 0$). The data from the electrostatic sensors on the windward meridian are presented in table II which presents the same type of data as table I. Most of the data points from the electrostatic sensors found on the windward meridian ($\psi = 0$) were first presented in reference 6 with the same local flow-field calculations as were used in table I. Nearly the same windward meridian ($\psi = 0$) data are presented in reference 8 with about the same tabular data listed but with a few more data points than those presented in reference 6. The output from the electrostatic probes was examined and gave an indication as to whether the boundary layer was laminar, transitional, or turbulent. The transitional data are defined as output that was just on the threshold of transition detection. After study of the output from the electrostatic sensor on the windward meridian ($\psi = 0$) was completed, it was determined that much more data could be obtained by examining the output of the same sensors when they were $\pm 5^{\circ}$ from the windward meridian ($\psi = \pm 5^{\circ}$). These data at $\psi = \pm 5^{\circ}$ are presented in table III with the same type of data as presented in tables I and II. These data at $\psi = \pm 5^{\circ}$ are presented in reference 8 with no local flow-field or boundary-layer calculations but with just a tabulation of the location of the sensor, the vehicle angle of attack, the free-stream Mach number, and the type of boundary layer at the sensor. The data

from the electrostatic sensors for both $\psi = 0$ and $\psi = \pm 5^{\circ}$ are presented in reference 8 as "Measurements on the Windward Ray." The data listed in tables II and III produced a total of 124 laminar boundary-layer data points and a total of 33 transitional and turbulent boundary-layer data points. In addition to the data from the electrostatic sensors obtained at $\psi = 0$ and $\psi = \pm 5^{\circ}$ (tables II and III), much data were obtained from measurements from the sensors with values of ψ much greater than $\pm 5^{\circ}$ and are presented in table IV with the same type of data as presented in tables I to III. The restrictions to the type of data in table IV obtained "Off the Windward Ray" are described in detail in reference 8. The data found away from the windward meridian, as listed in table IV, produced a total of 69 transitional and turbulent boundary-layer data points and a total of 57 laminar data points. In reference 8 there are 232 data points from the electrostatic sensors for which no local flow-field or boundary-layer calculations were made. The results from local flow-field and boundary-layer calculations for these 232 data points are presented in tables III and IV.

CORRELATION OF TRANSITION DATA

The transition data from the acoustic sensors and a limited number of the electrostatic static sensors (located on the windward meridian) were presented in reference 6 in a correlation in the form of

$$\log_{10}\left(\frac{R_{e,\delta^*}}{R_l^{0.25}}\right) \tag{1}$$

plotted against local Mach number where R_{e,δ^*} is calculated by using the simplified local similarity formula given in reference 1 as

$$R_{e,\delta^*} = \left(\frac{2}{3}\frac{\rho_w \mu_w}{\rho_e u_e}\frac{\rho_e u_e x}{\mu_e}\right)^{1/2}\left(\frac{\gamma - 1}{2} M_e^{\,2}\theta_i + \frac{T_w}{T_e}\delta_i^*\right) \tag{2}$$

$\theta_i = 0.4696$ and $\delta_i^* = 1.217$. The correlating parameter (eq. (1)) in reference 6 also used equation (2) to determine the value of δ^*. All correlating parameters presented in this report use equation (2) to determine the value of R_{e,δ^*}. In figures 3 to 5 are shown correlations of the flight transition data, presented in tables I to IV and using the correlating parameter of equation (1) plotted as a function of the local Mach number. The data in figure 3 were obtained with acoustic sensors (see fig. 1) and the data show a nearly linear variation with local Mach number. The solid line indicates the best linear curve fit to 77 sharp-cone flight data points for cones at an angle of attack of 0° (originally presented in ref. 1 and used in ref. 6). The acoustic sensor data indicate transition at a

lower value of the correlating parameter than the line from the flight data points for the 0^{o} angle-of-attack cone, the difference being larger as the local Mach number decreases. A similar phenomenon was noted from wind-tunnel tests in references 9 and 10. It is likely that the data fell below the flight data points for the $\alpha = 0^{o}$ cone because of the extreme sensitivity of the acoustic sensors to noise in the transitional and turbulent boundary layer and because of the early onset of transition due to crossflow resulting from the cone being at an angle of attack. The fact that the data from the acoustic sensors fall below the linear fit to the flight data points for the $\alpha = 0^{o}$ cone indicates that these sensors give an indication of the early stages of transition which could be better termed as the onset of transition. Thus, the extreme sensitivity of the acoustic sensors to turbulence level in the boundary layer plus the crossflow on the cone results in the data being below the linear fit to the sharp cone flight data as indicated in figure 3.

A plot similar to that of figure 3 is shown in figure 4 for transition data obtained with electrostatic sensors. The data from the electrostatic sensors show a trend that is similar to the trend indicated by the acoustic sensors in figure 3; however, there is considerable scatter in the data. The solid line from the 78 sharp-cone data points is in the upper part of the data scatter and gives an approximate upper bound to the transition data. It is interesting to note that in figure 9(b) of reference 6 that at a local Mach number of about 6 the data began to drop from a linear curve given for the flight data points for the $\alpha = 0^{o}$ sharp cone. This same dropoff at a local Mach number of about 7 is noted for the transition data in figure 4 and again is attributed to the effect of angle of attack. In reference 6 additional data at local Mach numbers less than about 5 showed a marked decrease in the correlating parameter.

In figure 5 the laminar data points listed in tables I to IV are included with the transition data previously shown in figures 3 and 4. Above a Mach number of about 6.0, the transitional and turbulent data show a trend of being above the open symbol laminar boundary-layer points; this trend indicates that above a Mach number of 6, a fairing through the turbulent and transitional data points should be a good indication of where transition can be expected. In figure 5 it should be noted that the data from the acoustic sensors lie in the lower part of the turbulent data points. This again indicates the sensitivity of the acoustic sensor which detects transition at a lower value of the correlating parameter than the electrostatic sensors do.

At the time the correlation parameter (eq. (1)) in figures 3 to 5 and in reference 6 was being used, a new type of correlation was being developed. The new correlation was based on a statistical, parametric study, in which a computer program was used to take into account the combined effects of unit Reynolds number, Mach number, and boundary-layer wall-to-edge enthalpy ratio on the correlating parameters. A description of the

new method is given in references 2 and 3. The new method of correlating transition data was particularly successful in a correlation of the Reentry F transition data (see ref. 3) when the parameter

$$\log_{10}\left(\frac{R_{e,\delta^*}}{R_l^{0.3}}\right) \tag{3}$$

was plotted against F_2, where F_2 is defined as

$$F_2 = 0.70579 + 0.17929M_e + \left(0.3760 - 0.04234M_e\right)\frac{h_w}{h_e} + \left(-0.11602 + 0.02417M_e - 0.00111M_e^2\right)\left(\frac{h_w}{h_e}\right)^2 \tag{4}$$

The data correlations using $\log_{10}\left(\frac{R_{e,\delta^*}}{R_l^{0.3}}\right)$ and F_2 given in equation (4) are shown in figures 6 to 8, and are compared with a linear curve fit found in reference 3 for two sets of flight data. The equation for the faired curve is

$$\log_{10}\left(\frac{R_{e,\delta^*}}{R_l^{0.3}}\right) = 0.81645F_2 + 0.4117 \tag{5}$$

where $l = 1$ meter. The slight difference in equation (5) and the equation found in reference 3 is a result of the l used in the correlating parameter of reference 3 being equal to 0.3048 meter (1 foot). The data in figures 6 to 8 are again taken from the data in tables I to IV. The turbulent and transitional boundary-layer data from the acoustic sensors are shown in figure 6, and, as was found in figure 3, show a linear variation with F_2. In addition, the data fall below the curve fit of equation (4) which again indicates the sensitivity of the acoustic sensors to the onset of transition. In figure 7 are shown the transitional and turbulent data from the electrostatic sensors. These data from the electrostatic sensors, as previously noted in figure 4, tend to scatter more than the data from the acoustic sensor. However, the data tend to scatter above and below the curve fit from equation (4). It should be noted that the data in figure 7 did not show a significant increase in slope in the low range of value of F_2, unlike the data in figure 4 which showed a marked increase in slope below a Mach number of approximately 6. However, the data in figure 7 indicate that for a value of F_2 less than about 2.0, the scattering of the data tends to show a slight increase in slope.

In figure 8 the laminar data points from tables I to IV are combined with the turbulent and transitional data from figures 6 and 7. There is a trend in figure 8 for the

transitional and turbulent data points to have a higher value than the open-symbol laminar data points for a value of F_2 greater than approximately 2.0. Below an F_2 of 2.0, the turbulent and laminar points are mixed.

The data for the third correlation, taken from tables I to IV, are shown in figures 9 to 11 and were based on the free-flight correlation of reference 2 in which the transition parameter

$$\log_{10}\left(\frac{R_{e,\delta^*}}{R_l^{\,n}}\right) \qquad (n = 0.275) \tag{6}$$

was plotted against F_2 where F_2 as given in reference 2 is

$$F_2 = 0.73825 + 0.19448M_e + \left(0.41157 - 0.04649M_e\right)\frac{h_w}{h_e} + \left(-0.07275 + 0.008712M_e\right)\left(\frac{h_w}{h_e}\right)^2 \tag{7}$$

These coefficients gave the lowest standard deviation from a least-squares curve fit of the data (that is, $\sigma_x = 0.141$) (with l equal to 0.3048 m (1 ft)). Also given in reference 2 is a linear curve fit of the transition parameter as a function of F_2 given by

$$\log_{10}\left(\frac{R_{e,\delta^*}}{R_l^{\,0.275}}\right) = 0.75352 + 0.74794F_2 \tag{8}$$

where l is equal to 0.3048 m (1 ft).

In figure 9 the transition data from the acoustic sensors fall slightly below the linear curve fit of the transition data (eq. (8) between values of F_2 of approximately 2.2 to 2.8). For values of F_2 less than approximately 2.2, the data fall increasingly below the linear fit of equation (8) as F_2 decreases. The fact that the data from the acoustic sensors fall below the linear fit to the 77 flight data points from reference 2 again indicates that the data from the acoustic sensors are very sensitive to the onset of transition.

The data in figure 10 are from electrostatic sensors where the transitional data are indicated by the diamond symbols and the fully turbulent data points are indicated by the circles with crosses in them. In general, the transitional data are in the lower part of the scattering of the turbulent data. Data from the electrostatic sensors show good agreement with the linear curve fit of equation (8), which is based on the 77 flight data points from reference 2, with the exception of a few points with values of F_2 less than about 2.2.

A comparison of the linear curve fits of the transitional and turbulent data in figures 7 and 10 (eqs. (5) and (8), respectively) indicates that equation (8) gives the best fit to the data.

In figure 11 are shown the transitional and turbulent data as well as the laminar data from both the acoustic as well as the electrostatic sensors. Again, the laminar data, indicated by the open symbols, in general fall below the transitional and turbulent data points as was previously indicated in figures 5 and 8. For values of F_2 from 2.2 to 2.8 the linear curve fit (eq. (8)) from the 77 flight data points from reference 2 appears to be the approximate dividing line between laminar and turbulent (and transitional) data. Below a value of F_2 of about 2.2 the laminar and turbulent data are mixed with the linear curve fit from reference 2 going through the data. Below a value of F_2 of about 2.0, the lowest data points are almost all laminar and fall well below the linear curve fit to the flight data. It can be inferred, from within the scatter of the data, that above a value of F_2 of about 1.8, the effect of angle of attack is negligible when the data are compared with the linear curve fit (eq. (8)) which was obtained from data predominately at an angle of attack of 0°. For the limited amount of transition data below a value of F_2 of 1.8, there is an effect of angle of attack which causes transition to occur at a lower angle of the correlating parameter.

CONCLUDING REMARKS

Additional points of transition data from a flight experiment which used a cone that reentered at high angles of attack were analyzed and their local flow conditions were presented. Laminar, transitional, and turbulent boundary-layer data from both acoustic and electrostatic sensors on the flight cone have been presented previously; however, the local flow conditions for the electrostatic sensors have only been presented for conditions when the electrostatic sensor was on the windward meridian. Presented herein in tabular form are the previously unpublished local flow conditions for the 93 transitional and turbulent data points and the 139 laminar data points. The tables of local conditions include angle of attack, Mach number, and Reynolds number based on axial distance, momentum thickness, and displacement thickness.

The data from the acoustic and electrostatic sensors were correlated by use of three different sets of correlating parameters. For each set of correlating parameters, the transitional and turbulent data from the acoustic and electrostatic sensors were plotted in separate correlations. In a third correlation all the data from both sensors including laminar, transitional, and turbulent data were plotted for the three sets of correlating parameters. For most of the data in the combined plots, the laminar data tended to fall

below the transitional and turbulent data and gave a reasonably clear indication of where transition can be expected to occur.

Each of the 9 correlations of the data was compared with a linear curve fit of approximately 77 flight data points at an angle of attack of approximately 0^{o}. In every instance the transition data from the acoustic sensors showed a linear variation with the correlating parameters but the data from the acoustic sensors fell below the linear curve fit of the flight data. In addition the transition data from the acoustic sensors fell in the lower region of the scattering of the data from the electrostatic sensors. These two aspects of the data from the acoustic sensors indicated that they were very sensitive to the noise in the boundary layer and that they were more likely detecting the onset of transition rather than a fully developed turbulent flow.

The transitional and turbulent data from the electrostatic sensors, which outnumbered the data from the acoustic sensors by a ratio of 102 to 16 tended to scatter much more than the acoustic sensor data. However, the data from the electrostatic sensors tended to scatter about the linear curve fits based on previous flight data. At lower values of the correlating parameter the data from the electrostatic sensors tended to show a dropoff from the linear curve fits from the other flight data. This dropoff (that is, an increase in slope within the scatter of the data) in the data was attributed to the effect of angle of attack and was most noticeable when the correlating parameter was plotted against Mach number. In general, when the correlating parameter was plotted against the parameter with the matrix coefficients, most of the data tended to scatter about the linear curve fits from previous flight data, with just a slight dropoff at the lower values of the correlating parameters. A comparison of the data with two linear correlations of the parameter with matrix coefficient indicated that the correlation of reference 2 showed the closest agreement with the data.

Langley Research Center
National Aeronautics and Space Administration
Hampton, Va. 23665
May 23, 1975

REFERENCES

1. Beckwith, Ivan E.; and Bertram, Mitchel H.: NASA Langley Studies on Stability and Transition in High-Speed Shear Layers. Proceedings of the Boundary Layer Transition Workshop held 3-5 November 1971, Volume I, W. D. McCauley, [ed.], Rep. No. TOR-0172 (S2816-16)-5 (Contract No. F04701-71-C-0172), Aerospace Corp., Dec. 20, 1971, pp. 5-1 – 5-70.

2. Beckwith, Ivan E.; and Bertram, Mitchel H.: A Survey of NASA Langley Studies on High-Speed Transition and the Quiet Tunnel. NASA TM X-2566, 1972.

3. Johnson, Charles B.; Stainback, P. Calvin; Wicker, Kathleen C.; and Boney, Lillian R.: Boundary-Layer Edge Conditions and Transition Reynolds Number Data for a Flight Test at Mach 20 (Reentry F). NASA TM X-2584, 1972.

4. Matthews, R. K.; Martindale, W. R.; Warmbrod, J.; and Johnson, C. B.: Heat Transfer Investigation of Langley Research Center Transition Models at a Mach Number of 8. NASA CR-120045, 1972.

5. Eaves, R. H.; Buchanan, T. D.; Warmbrod, J. D.; and Johnson, C. B.: Heat Transfer Investigations of Two Langley Research Center Delta Wing Configurations at a Mach Number of 10.5. NASA CR-120036, 1972.

6. Johnson, Charles B. (with appendix B by George C. Ashby, Jr.): Boundary-Layer Transition and Heating Criteria Applicable to Space Shuttle Configurations From Flight and Ground Tests. Vol. I of NASA Space Shuttle Technology Conference, NASA TM X-2272, 1971, pp. 97-156.

7. Haigh, Wayne W.; Lake, Bruce W.; and Ko, Denny R. S.: Addendum for Analysis of Flight Data on Boundary Layer Transition at High Angles-of-Attack. NASA CR-1914, 1973.

8. Haigh, Wayne W.; Lake, Bruce M.; and Ko, Denny R. S.: Analysis of Flight Data on Boundary Layer Transition at High Angles of Attack. NASA CR-1913, 1972.

9. Fischer, Michael C.; and Weinstein, Leonard M.: Cone Transitional Boundary-Layer Structure at $M_e = 14$. AIAA J., vol. 10, no. 5, May 1972, pp. 699-701.

10. Martellucci, A.; Chaump, L.; Rogers, D.; and Smith, D.: Experimental Determination of the Aero-Acoustic Environment About a Slender Cone. AIAA Paper No. 72-706, June 1972.

TABLE I.- DATA FROM ACOUSTIC SENSORS

x, meter	ψ, deg	Azimuth angle, Φ	Boundary-layer type	M_∞	α_{ℓ}, deg	M_e	$R_{e,x}$	$R_{e,\theta}$	$\overline{R}_{e,\delta^*}$	α, deg
2.235	0	101	Turbulent	20.83	22.78	3.67	4.09×10^5	171.9	4.629×10^2	30.83
↓	0	101	Turbulent	21.28	15.35	5.00	1.51×10^6	366.0	1.829×10^3	23.35
	0	101	Transitional	21.42	3.29	9.83	6.59×10^6	935.0	1.806×10^4	11.29
	0	101	Transitional	21.52	6.13	8.15	6.33×10^6	869.3	1.154×10^4	14.13
	0	101	Laminar	21.08	4.03	9.29	3.49×10^6	668.9	1.155×10^4	12.03
	-13.0	101	Turbulent	20.82	20.70	4.07	4.72×10^5	190.0	6.300×10^2	28.20
	117.9	101	Turbulent	21.47	12.30	18.80	1.12×10^7	1.92×10^3	8.980×10^4	2.20
↓	-35.5	101	Turbulent	21.50	13.90	6.11	3.66×10^6	618.0	4.490×10^3	19.30
4.216	0	110	Turbulent	21.29	15.97	4.86	2.77×10^6	492.1	2.329×10^3	23.97
↓	0	110	Transitional	20.83	22.76	3.67	7.80×10^5	236.4	6.379×10^2	30.76
	0	110	Transitional	21.09	3.84	9.43	5.94×10^6	875.0	1.556×10^4	11.84
	62.7	110	Turbulent	20.78	19.25	7.04	1.60×10^6	450.0	3.860×10^3	16.83
	-27.25	110	Turbulent	20.81	19.49	4.61	1.09×10^6	305.0	1.270×10^3	25.32
	43.7	290	Turbulent	20.98	16.84	5.86	2.27×10^6	485.0	3.150×10^3	20.17
	58.6	290	Turbulent	21.01	19.72	6.52	2.82×10^6	577.0	4.280×10^3	18.28
	-34.6	290	Turbulent	21.17	17.18	5.33	2.62×10^6	500.0	2.740×10^3	22.13
↓	-43.9	290	Turbulent	21.16	18.43	5.59	2.80×10^6	532.0	3.140×10^3	21.29

TABLE II.- DATA ON THE WINDWARD MERIDIAN (ELECTROSTATIC SENSORS)

x, meter	ψ, deg	Azimuth angle, Φ	Boundary-layer type	M_∞	α_t, deg	M_e	$R_{e,x}$	$R_{e,\theta}$	$\overline{R}_{e,\delta^*}$	α, deg
0.832	0	0	Laminar	20.40	11.64	5.96	2.00×10^5	141.8	9.925×10^2	19.64
↓	↓	0	Laminar	20.48	4.97	8.62	5.54×10^5	263.2	3.910×10^2	12.97
		0	Laminar	21.58	13.50	5.45	8.22×10^5	279.5	1.659×10^3	21.50
		0	Laminar	21.76	3.90	9.42	2.70×10^6	592.0	1.052×10^4	11.90
		0	Laminar	22.00	2.90	10.15	4.15×10^6	746.8	1.539×10^4	10.90
		0	Laminar	22.20	9.64	6.65	2.63×10^6	532.2	4.713×10^3	17.64
1.207		0	Laminar	20.40	11.63	5.93	2.91×10^5	171.1	1.201×10^3	19.63
↓		0	Laminar	20.48	4.97	8.64	8.06×10^5	317.6	4.738×10^3	12.97
		0	Laminar	21.76	3.90	9.44	3.92×10^6	713.8	1.271×10^4	11.90
		0	Laminar	22.00	2.90	10.16	6.02×10^6	900.4	1.860×10^4	10.90
		0	Transitional	22.20	9.64	6.66	3.82×10^6	641.3	5.685×10^3	17.64
2.235		0	Laminar	20.57	27.00	3.13	1.08×10^5	83.1	1.630×10^2	35.00
↓		0	Laminar	20.40	11.63	5.93	5.41×10^5	233.3	1.643×10^3	19.63
		0	Laminar	20.48	4.97	8.66	1.50×10^6	433.3	6.500×10^3	12.97
		0	Laminar	21.76	3.90	9.45	7.28×10^5	972.9	1.738×10^4	11.90
		0	Turbulent	22.00	2.90	10.18	1.12×10^7	1.227×10^3	2.543×10^4	10.90
.832		180	Laminar	23.70	13.81	5.31	1.27×10^4	34.5	1.943×10^2	21.81
↓		180	Laminar	21.00	6.82	7.66	1.29×10^5	123.4	1.447×10^3	14.82
		180	Laminar	20.42	6.78	7.68	2.21×10^5	161.3	1.901×10^3	14.78
		180	Laminar	20.61	7.60	7.37	5.04×10^5	248.9	2.701×10^3	15.60
		180	Laminar	20.91	6.05	8.11	9.26×10^5	334.3	4.397×10^3	14.05
		180	Laminar	21.45	4.16	9.22	1.73×10^6	471.9	8.019×10^3	12.16
		180	Laminar	21.65	8.98	6.87	1.38×10^6	389.2	3.678×10^3	16.98
		180	Laminar	21.89	2.57	10.38	3.69×10^6	709.2	1.528×10^4	10.57
		180	Laminar	22.10	5.25	8.64	3.70×10^6	677.9	1.013×10^4	13.25
1.702		180	Laminar	21.00	6.82	7.70	2.67×10^5	177.4	2.103×10^4	14.82
↓		180	Laminar	20.61	7.60	7.38	1.11×10^6	356.8	3.891×10^3	15.60
		180	Laminar	20.91	6.05	8.13	1.90×10^6	479.3	6.335×10^3	14.05
		180	Laminar	21.45	4.16	9.24	3.55×10^6	676.5	1.156×10^4	12.16
		180	Laminar	21.89	2.57	10.40	7.58×10^6	1.016×10^3	2.201×10^4	10.57
		180	Transitional	22.10	5.25	8.65	7.58×10^6	971.0	1.455×10^4	13.25
3.531		180	Laminar	23.70	13.81	5.36	5.48×10^4	71.9	4.132×10^2	21.81
↓		180	Laminar	21.00	6.82	7.73	5.58×10^5	256.4	3.064×10^3	14.82
		180	Laminar	20.42	6.78	7.73	9.51×10^5	334.6	4.001×10^3	14.78
		180	Laminar	20.61	7.60	7.40	2.31×10^5	514.8	5.633×10^3	15.60
		180	Laminar	20.91	6.05	8.14	3.96×10^6	691.5	9.171×10^3	14.05
		180	Laminar	21.45	4.16	9.26	7.39×10^6	975.9	1.674×10^4	12.16
		180	Turbulent	21.89	2.57	10.42	1.58×10^7	1.466×10^3	3.186×10^4	10.57
		180	Transitional	22.10	5.25	8.66	1.58×10^7	1.400×10^3	2.103×10^4	13.25
4.216		180	Laminar	23.70	13.81	5.37	6.56×10^4	78.6	4.528×10^2	21.81
↓		180	Laminar	21.00	6.82	7.73	6.68×10^5	280.4	3.356×10^3	14.82
		180	Laminar	20.42	6.78	7.74	1.14×10^6	365.8	4.380×10^3	14.78
		180	Laminar	20.61	7.60	7.40	2.76×10^6	562.7	6.162×10^3	15.60
		180	Laminar	20.91	6.05	8.15	4.73×10^6	755.9	1.003×10^4	14.05
		180	Laminar	21.45	4.16	9.26	8.82×10^6	1.067×10^3	1.831×10^4	12.16
		180	Turbulent	21.89	2.57	10.43	1.88×10^7	1.602×10^3	3.485×10^4	10.57
		180	Turbulent	22.10	5.25	8.67	1.88×10^7	1.530×10^3	2.299×10^4	13.25
		150	Laminar	20.41	12.88	5.59	1.01×10^5	313.2	1.956×10^3	20.88
		150	Laminar	20.90	4.08	9.26	5.71×10^6	858.8	1.472×10^4	12.08
		150	Turbulent	21.43	7.99	7.28	5.82×10^6	812.6	8.612×10^3	15.99
↓	↓	150	Turbulent	21.88	2.74	10.30	1.84×10^7	1.579×10^3	3.348×10^4	10.74

TABLE III.- DATA NEAR THE WINDWARD MERIDIAN (ELECTROSTATIC SENSORS)

x, meter	ψ, deg	Azimuth angle, Φ	Boundary-layer type	M_∞	α_t, deg	M_e	$R_{e,x}$	$R_{e,\theta}$	$\overline{R}_{e,\delta^*}$	α, deg
0.832	+7.0	0	Laminar	20.75	25.45	3.34	4.33×10^4	54.0	1.20×10^2	33.30
	-5.0	0	Laminar	20.87	12.80	5.61	1.65×10^5	126.5	7.96×10^2	20.90
	-5.0	0	Laminar	20.48	4.80	8.72	5.37×10^5	206.0	3.594×10^3	13.00
	+5.0	0	Laminar	20.50	5.17	8.52	5.32×10^5	257.1	3.733×10^3	13.30
	-5.0	0	Laminar	21.56	15.20	5.05	7.08×10^5	253.2	1.289×10^3	23.20
	+5.0	0	Laminar	21.55	12.10	5.85	9.09×10^5	300.9	2.054×10^3	20.10
	-5.0	0	Laminar	21.70	3.70	9.56	2.53×10^6	575.8	1.052×10^4	11.80
	+5.0	0	Laminar	21.70	4.20	9.23	2.40×10^6	555.9	9.480×10^3	12.30
	-5.0	0	Laminar	21.96	3.10	10.00	3.81×10^6	713.6	1.429×10^4	11.20
	+5.0	0	Laminar	21.96	2.80	10.22	3.93×10^6	729.1	1.524×10^4	10.90
	-5.0	0	Laminar	22.25	10.14	6.49	2.52×10^6	517.2	4.358×10^3	18.10
	+5.0	0	Laminar	22.27	8.87	6.96	2.95×10^6	570.9	5.532×10^3	16.90
1.207	-5.0	0	Laminar	20.87	12.80	5.62	2.39×10^5	152.6	9.627×10^2	20.90
	+5.0	0	Laminar	20.40	10.60	6.26	3.15×10^5	181.2	1.418×10^3	18.70
	-5.0	0	Laminar	20.48	4.80	8.74	7.81×10^5	313.7	4.792×10^3	12.90
	+5.0	0	Laminar	20.50	5.17	8.54	7.73×10^5	310.2	4.523×10^3	13.30
	+5.0	0	Laminar	21.55	12.10	5.85	1.32×10^6	362.6	2.479×10^3	20.10
	-5.0	0	Laminar	21.70	3.70	9.57	3.68×10^6	694.2	1.271×10^4	11.80
	+5.0	0	Laminar	21.70	4.20	9.24	3.49×10^6	670.2	1.146×10^4	12.30
	-5.0	0	Laminar	21.96	3.10	10.02	5.53×10^6	860.3	1.727×10^4	11.20
	+5.0	0	Transitional	21.96	2.80	10.24	5.72×10^6	878.9	1.843×10^4	10.90
	-5.0	0	Turbulent	22.25	10.14	6.49	3.66×10^6	623.1	5.255×10^3	18.10
	+5.0	0	Turbulent	22.27	8.87	6.96	4.28×10^6	687.9	6.672×10^3	16.90
2.235	-5.0	0	Laminar	20.87	12.80	5.63	4.45×10^5	208.0	1.316×10^3	20.80
	+5.0	0	Laminar	20.40	10.60	6.27	5.86×10^5	247.1	1.940×10^3	18.60
	-5.0	0	Laminar	20.48	4.80	8.77	1.45×10^6	428.1	6.577×10^3	12.90
	+5.0	0	Laminar	20.50	5.17	8.56	1.44×10^6	423.2	6.205×10^3	13.30
	+5.0	0	Laminar	21.55	12.10	5.85	2.44×10^6	493.4	3.381×10^3	20.00
	-5.0	0	Laminar	21.70	3.70	9.59	6.83×10^6	946.3	1.739×10^4	11.76
	+5.0	0	Turbulent	21.70	4.20	9.26	6.48×10^6	913.4	1.567×10^4	12.25
	-5.0	0	Turbulent	21.96	3.10	10.04	1.03×10^7	1.172×10^3	2.362×10^4	11.15
	+5.0	0	Turbulent	21.96	2.80	10.26	1.06×10^7	1.198×10^3	2.521×10^4	10.86
	+5.0	0	Transitional	22.27	8.87	6.97	7.94×10^6	937.0	9.100×10^3	16.90
.832	-5.0	180	Laminar	23.70	13.18	5.47	1.31×10^4	35.5	212.8	21.60
	+5.0	180	Laminar	23.63	14.52	5.15	1.21×10^4	33.4	177.1	22.90
	-5.0	180	Laminar	20.86	6.81	7.67	1.40×10^5	128.6	1.512×10^3	15.10
	+5.0	180	Laminar	20.90	6.87	7.65	1.41×10^5	128.6	1.503×10^3	15.10
	-5.0	180	Laminar	20.40	6.48	7.82	2.26×10^5	163.9	2.005×10^3	14.70
	+5.0	180	Laminar	20.45	7.14	7.53	2.14×10^5	157.8	1.789×10^3	15.30
	-5.0	180	Laminar	20.63	8.25	7.11	5.21×10^5	242.0	2.448×10^3	16.30
	+5.0	180	Laminar	20.61	7.10	7.60	5.92×10^5	262.7	3.032×10^3	15.20
	-5.0	180	Laminar	20.95	5.50	8.40	9.62×10^5	344.2	4.863×10^3	13.60
	+5.0	180	Laminar	20.92	6.75	7.78	8.84×10^5	323.1	3.915×10^3	14.80
	-5.0	180	Laminar	21.45	4.50	9.02	1.66×10^6	461.0	7.500×10^3	12.60
	+5.0	180	Laminar	21.43	3.90	9.39	1.82×10^6	486.7	8.583×10^3	12.00
	-5.0	180	Laminar	21.66	8.00	7.28	1.56×10^6	421.5	4.468×10^3	16.00
	-5.0	180	Laminar	21.90	2.55	10.40	3.75×10^6	715.9	1.550×10^3	10.70
	+5.0	180	Laminar	21.89	2.62	10.35	3.76×10^6	715.2	1.532×10^3	10.70
	-5.0	180	Laminar	22.10	5.92	8.29	3.50×10^6	652.8	8.971×10^3	14.00
	+5.0	180	Laminar	22.10	4.75	8.94	4.01×10^6	712.1	1.139×10^4	12.80
1.702	+5.0	180	Laminar	23.63	14.52	5.18	2.50×10^4	48.1	257.8	22.70
	-5.0	180	Laminar	20.86	6.81	7.71	2.89×10^5	184.8	2.197×10^3	15.00
	+5.0	180	Laminar	20.90	6.87	7.69	2.90×10^5	184.8	2.183×10^3	15.00

TABLE III.- DATA NEAR THE WINDWARD MERIDIAN (ELECTROSTATIC SENSORS) – Concluded

x, meter	ψ, deg	Azimuth angle, Φ	Boundary-layer type	M_∞	α_t, deg	M_e	$R_{e,x}$	$R_{e,\theta}$	$\overline{R}_{e,\delta^*}$	α, deg
1.702	-5.0	180	Laminar	20.63	8.25	7.13	1.07×10^6	346.8	3.524×10^3	16.30
	+5.0	180	Laminar	20.61	7.10	7.62	1.22×10^6	376.7	4.369×10^3	15.20
	-5.0	180	Laminar	20.95	5.50	8.43	1.98×10^6	493.5	7.010×10^3	13.60
	+5.0	180	Laminar	20.92	6.75	7.80	1.82×10^6	463.1	5.636×10^3	14.80
	-5.0	180	Laminar	21.45	4.50	9.04	3.42×10^6	660.8	1.081×10^4	12.60
	+5.0	180	Laminar	21.43	3.90	9.42	3.74×10^6	697.7	1.237×10^4	12.00
	-5.0	180	Laminar	21.66	8.00	7.29	3.21×10^6	603.7	6.419×10^3	16.00
	-5.0	180	Laminar	21.90	2.55	10.43	7.72×10^6	1.025×10^3	2.232×10^4	10.60
	+5.0	180	Laminar	21.89	2.62	10.69	7.72×10^6	1.024×10^3	2.206×10^4	10.70
	-5.0	180	Transitional	22.10	5.95	8.28	7.16×10^6	933.1	1.281×10^4	14.00
↓	+5.0	180	Transitional	22.10	4.75	8.96	8.22×10^6	1.020×10^3	1.638×10^4	12.80
3.531	-5.0	180	Laminar	23.70	13.18	5.53	5.69×10^4	74.1	453.8	21.30
	+5.0	180	Laminar	23.63	14.52	5.20	5.24×10^4	69.6	376.1	22.70
	-5.0	180	Laminar	20.86	6.81	7.74	6.05×10^5	267.1	3.201×10^3	14.90
	+5.0	180	Laminar	20.90	6.87	7.72	6.06×10^5	267.1	3.179×10^3	15.00
	-5.0	180	Laminar	20.40	6.48	7.88	9.70×10^5	339.9	4.223×10^3	14.60
	+5.0	180	Laminar	20.45	7.14	7.58	9.19×10^5	327.2	3.762×10^3	15.20
	-5.0	180	Laminar	20.63	8.25	7.14	2.23×10^6	500.3	5.101×10^3	16.30
	+5.0	180	Laminar	20.61	7.10	7.63	2.53×10^6	543.5	6.327×10^3	15.10
	-5.0	180	Laminar	20.95	5.50	8.44	4.12×10^6	712.0	1.015×10^4	13.50
	+5.0	180	Laminar	20.92	6.75	7.81	3.78×10^6	668.0	8.157×10^3	14.80
	-5.0	180	Laminar	21.45	4.50	9.06	7.13×10^6	953.2	1.565×10^4	12.50
	+5.0	180	Laminar	21.43	3.90	9.43	7.79×10^6	1.006×10^3	1.792×10^4	11.90
	-5.0	180	Turbulent	21.90	2.55	10.45	1.60×10^7	1.479×10^3	3.230×10^4	10.60
	+5.0	180	Turbulent	21.89	2.62	10.39	1.61×10^7	1.477×10^3	3.193×10^4	10.70
	-5.0	180	Transitional	22.10	5.95	8.29	1.49×10^7	1.345×10^3	1.850×10^4	13.90
↓	+5.0	180	Transitional	22.10	4.75	8.97	1.71×10^7	1.471×10^3	2.367×10^4	12.80
4.216	-5.0	180	Laminar	23.70	13.18	5.54	6.81×10^4	81.0	497.3	21.30
	+5.0	180	Laminar	23.63	14.52	5.20	6.27×10^4	76.1	412.0	22.60
	-5.0	180	Laminar	20.86	6.81	7.75	7.24×10^5	292.1	3.505×10^3	14.90
	+5.0	180	Laminar	20.90	6.87	7.22	7.25×10^5	292.0	3.482×10^3	15.00
	-5.0	180	Laminar	20.40	6.48	7.89	1.16×10^6	371.6	4.623×10^3	14.60
	-5.0	180	Laminar	20.63	8.25	7.14	2.66×10^6	546.9	5.579×10^3	16.30
	+5.0	180	Laminar	20.91	7.10	7.65	3.07×10^6	598.4	7.001×10^3	15.10
	-5.0	180	Laminar	20.95	5.50	8.45	4.91×10^6	778.4	1.111×10^4	13.50
	+5.0	180	Laminar	20.92	6.75	7.82	4.51×10^6	730.2	8.922×10^3	14.80
	-5.0	180	Laminar	21.45	4.50	9.06	8.51×10^6	1.041×10^3	1.711×10^4	12.50
	+5.0	180	Laminar	21.43	3.90	9.44	9.30×10^6	1.100×10^3	1.960×10^4	11.90
	-5.0	180	Turbulent	21.90	2.55	10.45	1.92×10^7	1.617×10^3	3.533×10^4	10.60
	+5.0	180	Turbulent	21.89	2.62	10.40	1.92×10^7	1.615×10^3	3.492×10^4	10.70
	-5.0	180	Turbulent	22.10	5.95	8.29	1.78×10^7	1.470×10^3	2.023×10^4	13.90
	+5.0	180	Transitional	22.10	4.75	8.97	2.04×10^7	1.608×10^3	2.588×10^4	12.80
	+5.0	150	Laminar	20.40	14.15	5.27	9.11×10^5	291.6	1.622×10^3	22.14
	-5.0	150	Laminar	20.60	15.00	5.08	1.46×10^6	364.9	1.883×10^3	23.00
	+6.0	150	Laminar	20.60	11.97	5.87	1.95×10^6	440.7	3.031×10^3	20.00
	-5.0	150	Laminar	20.95	3.96	9.35	5.82×10^6	869.0	1.518×10^4	12.00
	-5.0	150	Turbulent	21.40	9.17	6.82	5.08×10^6	745.0	6.931×10^3	17.20
	+5.0	150	Turbulent	21.40	6.90	7.78	6.34×10^6	863.8	1.044×10^4	14.90
	-5.0	150	Turbulent	21.63	4.42	9.12	1.09×10^7	1.182×10^3	1.971×10^4	12.50
	-5.0	150	Turbulent	21.85	2.84	10.23	1.79×10^7	1.554×10^3	3.252×10^4	10.90
	+5.0	150	Turbulent	21.85	2.66	10.36	1.83×10^7	1.575×10^3	3.382×10^4	10.70
	-5.0	150	Turbulent	22.05	11.60	6.02	9.51×10^6	981.4	7.107×10^3	19.60
↓	+7.0	150	Turbulent	22.10	10.40	6.42	1.09×10^6	1.073×10^3	8.844×10^3	18.30

TABLE IV.- DATA AWAY FROM THE WINDWARD MERIDIAN (ELECTROSTATIC SENSORS)

x, meter	ψ, deg	Azimuth angle, Φ	Boundary-layer type	M_∞	α_t, deg	M_e	$R_{e,x}$	$R_{e,\theta}$	$\overline{R}_{e,\delta^*}$	α, deg
0.832	-30.09	180	Transitional	20.60	13.45	5.94	3.95×10^5	201.6	1.399×10^3	19.70
↓	-25.42	180	Transitional	20.60	12.06	6.17	4.21×10^5	210.0	1.578×10^3	18.90
↓	-19.68	180	Transitional	20.60	10.71	6.42	4.52×10^5	219.4	1.804×10^3	18.20
↓	+12.77	180	Transitional	20.60	9.43	6.74	4.90×10^5	231.2	2.095×10^3	17.30
1.207	-76.22	0	Turbulent	22.16	3.33	12.00	9.10×10^6	1.163×10^3	3.300×10^4	8.90
↓	-45.36	0	Turbulent	22.16	4.57	9.96	7.01×10^6	974.7	1.920×10^4	11.30
↓	-27.72	0	Turbulent	22.00	7.80	7.79	4.90×10^6	763.9	9.220×10^3	14.90
↓	-21.04	0	Turbulent	22.00	8.95	7.15	4.23×10^6	691.9	7.048×10^3	16.40
↓	-15.73	0	Transitional	22.00	9.88	6.70	3.79×10^6	641.0	5.741×10^3	17.50
1.702	+63.25	180	Laminar	20.45	14.94	7.76	8.97×10^5	346.2	3.768×10^3	14.80
↓	+68.34	180	Laminar	20.49	13.61	8.59	1.06×10^6	390.6	5.182×10^3	13.20
↓	+73.19	180	Transitional	20.50	12.25	9.43	1.23×10^6	434.6	6.962×10^3	11.80
↓	-30.09	180	Transitional	20.61	13.45	5.96	8.03×10^5	287.3	2.003×10^3	19.70
↓	-25.42	180	Turbulent	20.62	12.06	6.18	8.61×10^5	300.0	2.267×10^3	18.90
↓	-19.68	180	Turbulent	20.62	10.71	6.44	9.31×10^5	315.1	2.600×10^3	18.10
↓	-12.77	180	Transitional	20.63	9.43	6.75	1.02×10^6	333.1	3.033×10^3	17.30
↓	-38.36	180	Laminar	20.95	3.90	9.91	2.58×10^6	590.2	1.154×10^4	11.20
↓	-72.39	180	Laminar	21.66	3.29	11.67	6.31×10^6	964.1	2.608×10^4	9.11
↓	-83.12	180	Transitional	21.89	7.04	11.86	8.93×10^6	1.199×10^3	3.223×10^4	8.96
↓	-57.56	180	Transitional	21.90	3.73	10.86	8.06×10^6	1.068×10^3	2.502×10^4	10.09
↓	-24.77	180	Turbulent	21.91	2.66	10.53	7.79×10^6	1.034×10^3	2.290×10^4	10.50
↓	+20.50	180	Transitional	21.92	2.78	10.38	7.70×10^6	1.024×10^3	2.207×10^4	10.68
↓	+51.60	180	Transitional	21.92	3.92	10.51	7.91×10^6	1.049×10^3	2.306×10^4	10.51
↓	+68.20	180	Turbulent	21.93	5.61	10.80	7.79×10^6	1.100×10^3	2.512×10^4	10.16
↓	+79.07	180	Turbulent	21.93	7.37	11.37	9.00×10^6	1.191×10^3	2.944×10^4	9.49
↓	+88.35	180	Transitional	21.94	9.09	12.41	1.02×10^7	1.344×10^3	3.791×10^4	8.41
↓	-65.80	180	Turbulent	22.05	6.51	10.36	9.16×10^6	1.149×10^3	2.404×10^4	10.73
↓	-59.44	180	Turbulent	22.06	8.10	9.36	7.89×10^6	1.043×10^3	1.769×10^4	12.15
↓	-52.95	180	Turbulent	22.07	9.48	8.43	6.71×10^6	943.4	1.282×10^4	13.71
↓	-41.27	180	Turbulent	21.00	11.76	6.95	5.45×10^6	791.0	7.423×10^3	16.80
↓	-37.35	180	Turbulent	21.01	11.76	6.75	5.24×10^6	766.2	6.828×10^3	17.30
↓	-32.33	180	Turbulent	21.02	11.39	6.65	5.14×10^6	752.3	6.539×10^3	17.61
↓	-21.98	180	Turbulent	21.03	9.68	6.87	5.55×10^6	783.9	7.367×10^3	17.00
↓	-16.85	180	Turbulent	21.03	8.28	7.29	6.19×10^6	840.8	8.920×10^3	16.00
↓	-9.08	180	Turbulent	21.04	6.62	7.92	7.17×10^6	923.6	1.158×10^4	14.60
2.235	-34.49	0	Turbulent	20.70	14.49	5.90	1.18×10^7	1.102×10^3	7.478×10^3	19.80
↓	-9.39	0	Turbulent	21.58	15.88	4.94	1.87×10^6	408.7	1.987×10^3	23.70
↓	-5.49	0	Turbulent	21.59	15.35	5.02	1.94×10^6	418.8	2.110×10^3	23.30
↓	+43.65	0	Turbulent	21.80	9.61	7.74	5.84×10^6	843.7	9.884×10^3	14.90
↓	+48.66	0	Turbulent	21.81	10.91	7.67	5.47×10^6	820.8	9.320×10^3	15.20
↓	+53.15	0	Transitional	21.81	12.13	7.65	5.49×10^6	829.9	9.245×10^3	15.20
↓	+81.64	0	Turbulent	21.87	11.87	11.09	1.04×10^7	1.348×10^3	2.902×10^4	9.80
↓	+86.53	0	Transitional	21.87	10.53	12.06	1.78×10^7	1.459×10^3	3.774×10^4	8.75
↓	-43.10	0	Turbulent	22.02	6.55	8.93	9.05×10^6	1.083×10^3	1.710×10^4	12.82
↓	-31.48	0	Turbulent	22.03	4.80	9.36	9.85×10^6	1.133×10^3	1.978×10^4	12.14
↓	-8.96	0	Turbulent	22.04	3.16	10.02	1.11×10^7	1.215×10^3	2.441×10^4	11.18
↓	+37.60	0	Turbulent	22.05	2.45	10.94	1.27×10^7	1.332×10^3	3.184×10^4	10.01
3.531	-38.49	180	Turbulent	21.44	10.05	7.35	4.99×10^6	765.7	8.117×10^3	15.90
↓	-32.20	180	Laminar	21.44	8.50	7.64	5.32×10^6	794.6	9.179×10^3	15.20
↓	+44.87	180	Turbulent	21.45	3.12	10.64	9.37×10^6	1.141×10^3	2.576×10^4	10.30
↓	+82.72	180	Turbulent	21.45	3.61	12.17	1.12×10^7	1.302×10^3	3.815×10^4	8.50
4.216	+23.74	180	Transitional	21.00	10.78	6.55	3.39×10^6	605.2	5.146×10^3	17.90
↓	+33.04	180	Transitional	21.00	13.47	6.09	3.05×10^6	565.4	4.107×10^3	19.20
↓	+56.00	180	Laminar	21.07	19.10	6.38	3.42×10^6	630.2	4.576×10^3	18.40
↓	+56.90	180	Turbulent	21.10	19.10	6.47	3.57×10^6	647.4	4.807×10^3	18.10
↓	+59.30	180	Turbulent	21.11	18.98	6.73	3.84×10^6	683.8	5.427×10^3	17.40
↓	-75.64	180	Turbulent	21.36	15.74	9.50	7.93×10^6	1.138×10^3	1.696×10^4	11.80
↓	-72.08	180	Turbulent	21.37	16.03	8.89	7.60×10^6	1.080×10^3	1.438×10^4	12.80
↓	-68.47	180	Turbulent	21.38	15.92	8.39	6.98×10^6	1.005×10^3	1.220×10^4	13.70
↓	-56.53	180	Turbulent	21.40	14.85	7.27	5.64×10^6	838.6	8.200×10^3	16.00
↓	-52.48	180	Turbulent	21.40	14.01	7.12	5.48×10^6	814.1	7.760×10^3	16.40
↓	-84.13	150	Turbulent	20.40	5.96	11.72	3.08×10^6	697.1	1.850×10^4	8.80
↓	-66.06	150	Turbulent	20.40	6.01	10.27	2.62×10^6	613.5	1.265×10^4	10.60
↓	-62.18	150	Turbulent	21.33	12.93	8.24	6.50×10^6	940.2	1.183×10^4	14.00

TABLE IV.- DATA AWAY FROM THE WINDWARD MERIDIAN (ELECTROSTATIC SENSORS) – Concluded

x, meter	ψ, deg	Azimuth angle, Φ	Boundary-layer type	M_∞	α_t, deg	M_e	$R_{e,x}$	$R_{e,\theta}$	$\overline{R}_{e,\delta^*}$	α, deg
4.216	-57.63	150	Turbulent	21.33	13.85	7.59	5.66×10^6	851.4	9.120×10^3	15.30
↓	-53.22	150	Turbulent	21.34	14.69	7.02	5.01×10^6	776.9	7.152×10^3	16.70
	-38.47	150	Turbulent	21.38	15.92	5.78	3.70×10^6	615.7	3.950×10^3	20.30
	-26.53	150	Turbulent	21.40	14.85	5.23	3.51×10^6	585.2	3.519×10^3	21.20
↓	-22.48	150	Turbulent	21.40	14.01	5.61	3.64×10^6	597.3	3.723×10^3	20.90
0.832	-26.41	0	Laminar	24.44	32.40	2.93	3.06×10^3	13.60	21.95	37.00
1.207	-26.41	0	Laminar	24.44	32.40	2.94	4.47×10^3	16.46	26.78	36.90
2.235	-26.41	0	Laminar	24.44	32.40	2.96	8.35×10^3	22.54	37.04	36.80
2.235	+24.87	0	Laminar	22.48	33.66	2.82	2.44×10^4	37.69	56.19	38.10
.832	+29.20	0	Laminar	21.30	30.21	3.25	2.44×10^4	40.10	79.65	34.00
1.207	+29.20	0	Laminar	21.30	30.21	3.26	3.55×10^4	48.40	96.47	34.00
2.235	+29.20	0	Laminar	21.30	30.21	3.27	6.59×10^4	66.05	132.2	33.90
.832	+25.05	0	Laminar	20.51	18.99	4.59	8.21×10^4	84.05	347.2	25.20
1.207	+25.05	0	Laminar	20.51	18.99	4.60	1.19×10^5	101.4	419.8	25.20
2.235	+25.05	0	Laminar	20.51	18.99	4.61	2.22×10^5	138.3	574.8	25.20
.832	+47.45	0	Laminar	20.50	9.49	7.87	4.99×10^5	249.1	3.006×10^3	14.60
1.207	+47.45	0	Laminar	20.50	9.49	7.89	7.26×10^5	300.8	3.650×10^3	14.60
2.235	+47.45	0	Laminar	20.50	9.49	7.92	1.35×10^6	410.9	5.021×10^3	14.50
.832	+26.04	0	Laminar	20.84	12.91	5.96	5.16×10^5	229.7	1.614×10^3	19.70
1.207	+26.04	0	Laminar	20.84	12.91	5.97	7.49×10^5	227.0	1.949×10^3	19.60
2.235	+26.04	0	Laminar	20.84	12.91	5.98	1.39×10^6	377.5	2.664×10^3	19.60
.832	+87.82	0	Laminar	21.32	12.93	11.68	2.14×10^6	638.3	1.439×10^4	9.00
1.207	+87.82	0	Laminar	21.32	12.93	11.79	3.15×10^6	776.5	1.779×10^4	8.90
2.235	+87.82	0	Laminar	21.32	12.93	11.94	5.93×10^6	1.071×10^3	2.506×10^4	8.80
.832	-16.68	0	Laminar	21.56	16.66	4.87	6.70×10^5	244.1	1.151×10^3	24.00
1.207	-16.68	0	Laminar	21.56	16.66	4.87	9.73×10^5	294.1	1.387×10^3	23.90
.832	+53.15	0	Laminar	21.81	12.13	7.63	2.03×10^6	504.1	5.577×10^3	15.30
1.207	+53.15	0	Laminar	21.81	12.13	7.64	2.95×10^6	608.2	6.748×10^3	15.30
2.235	-53.15	0	Turbulent	21.81	12.13	7.65	5.49×10^6	829.7	9.243×10^3	15.20
.832	-56.27	0	Laminar	22.35	9.50	8.66	3.05×10^6	637.4	9.190×10^3	13.30
1.207	-56.27	0	Laminar	22.35	9.50	8.67	4.44×10^6	769.0	1.112×10^3	13.30
2.235	-56.27	0	Turbulent	22.35	9.50	8.69	8.26×10^6	1.049×10^3	1.524×10^3	13.30
.832	+41.33	180	Laminar	25.40	47.30	2.29	2.55×10^2	3.44	2.62	44.10
1.702	+41.33	180	Laminar	25.40	47.30	2.38	5.56×10^2	5.12	4.28	42.90
3.531	+41.33	180	Laminar	25.40	47.30	2.45	1.21×10^3	7.62	6.81	42.00
4.216	+41.33	180	Laminar	25.40	47.30	2.47	1.45×10^3	8.38	7.60	41.90
.832	+31.53	180	Laminar	23.35	19.91	4.59	1.11×10^4	30.84	125.5	25.40
1.702	+31.53	180	Laminar	23.35	19.91	4.63	2.28×10^4	44.56	184.5	25.20
3.531	+31.53	180	Laminar	23.35	19.91	4.66	4.78×10^4	64.67	271.0	25.10
4.216	+31.53	180	Laminar	23.35	19.91	4.66	5.72×10^4	70.78	297.4	25.00
.832	+44.74	180	Laminar	20.40	15.36	6.13	1.61×10^5	131.8	942.1	19.08
1.702	+44.74	180	Laminar	20.40	15.36	6.17	3.32×10^5	189.9	1.372×10^3	19.00
3.531	+44.74	180	Laminar	20.40	15.36	6.19	6.94×10^5	274.8	2.003×10^3	18.90
4.216	+44.74	180	Laminar	20.40	15.36	6.19	8.30×10^5	300.6	2.194×10^3	18.90
.832	+53.34	180	Laminar	20.45	17.16	6.54	3.24×10^5	194.7	1.520×10^3	17.80
1.702	+53.34	180	Laminar	20.45	17.16	6.59	6.70×10^5	280.8	2.220×10^3	17.70
3.531	+53.34	180	Laminar	20.45	17.16	6.62	1.40×10^6	406.9	3.249×10^3	17.60
4.216	+53.34	180	Laminar	20.45	17.16	6.63	1.68×10^6	445.1	3.561×10^3	17.60
.832	-38.93	180	Laminar	20.60	15.94	5.74	3.62×10^5	192.3	1.216×10^3	20.40
1.702	-38.93	180	Laminar	20.60	15.94	5.76	7.44×10^5	276.0	1.755×10^3	20.30
3.531	-38.93	180	Laminar	20.60	15.94	5.77	1.55×10^6	398.5	2.545×10^3	20.30
4.216	-38.93	180	Laminar	20.60	15.94	5.77	1.85×10^6	435.7	2.785×10^3	20.30
.832	-48.48	180	Laminar	21.40	12.88	7.06	1.08×10^6	356.7	3.395×10^3	16.60
1.702	-48.48	180	Laminar	21.40	12.88	7.08	2.21×10^6	511.9	4.901×10^3	16.50
3.531	-48.48	180	Transitional	21.40	12.88	7.10	4.61×10^6	739.3	7.110×10^3	16.50
4.216	-48.48	180	Turbulent	21.40	12.88	7.10	5.51×10^6	808.4	7.781×10^3	16.50
↓	+10.45	150	Laminar	25.40	36.01	2.33	8.74×10^2	6.63	7.09	43.60
	+32.84	150	Laminar	20.42	21.92	4.42	7.31×10^5	248.1	922.8	26.20
	-28.96	150	Laminar	20.56	21.75	4.30	1.06×10^6	295.6	1.054×10^3	26.80
	+53.75	150	Laminar	21.00	10.87	8.02	4.78×10^6	782.5	9.643×10^3	14.40
	-26.53	150	Turbulent	21.40	14.85	5.53	3.51×10^6	585.5	3.521×10^3	21.20
	+44.32	150	Turbulent	21.69	12.07	7.06	7.61×10^6	942.2	9.084×10^3	16.60
↓	-63.47	150	Turbulent	22.25	10.43	9.07	1.43×10^7	1.416×10^3	2.203×10^4	12.60

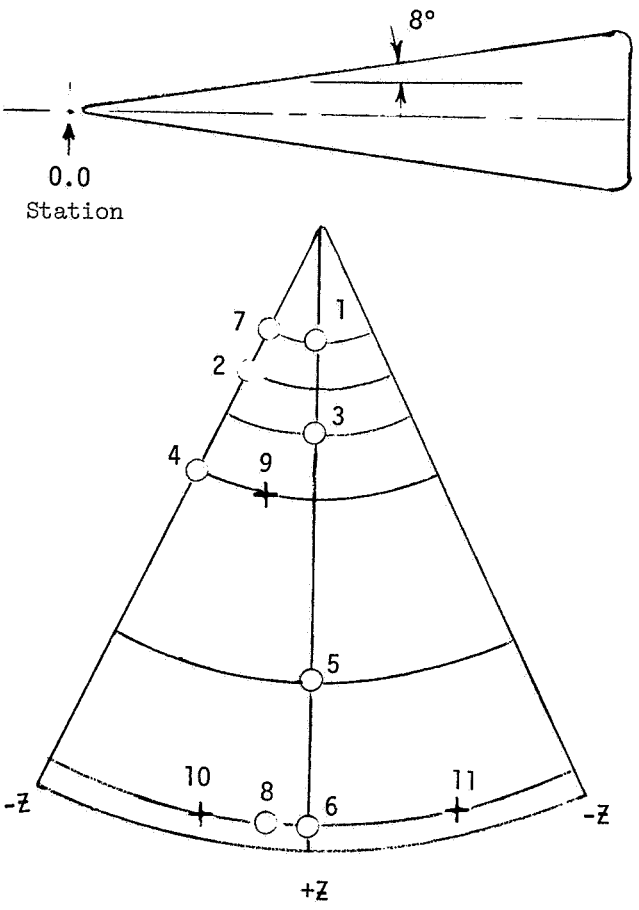

○ Electrostatic sensor

+ Acoustic sensor

Probe location	Axial station, m	Angle*, Φ, deg
1	0.832	180
2	1.194	0
3	1.702	180
4	2.235	0
5	3.531	180
6	4.216	180
7	0.832	0
8	4.216	150
9	2.235	101
10	4.216	110
11	4.216	290

*Clockwise from -Z axis, looking forward

Figure 1.- Instrumentation on flight configuration.

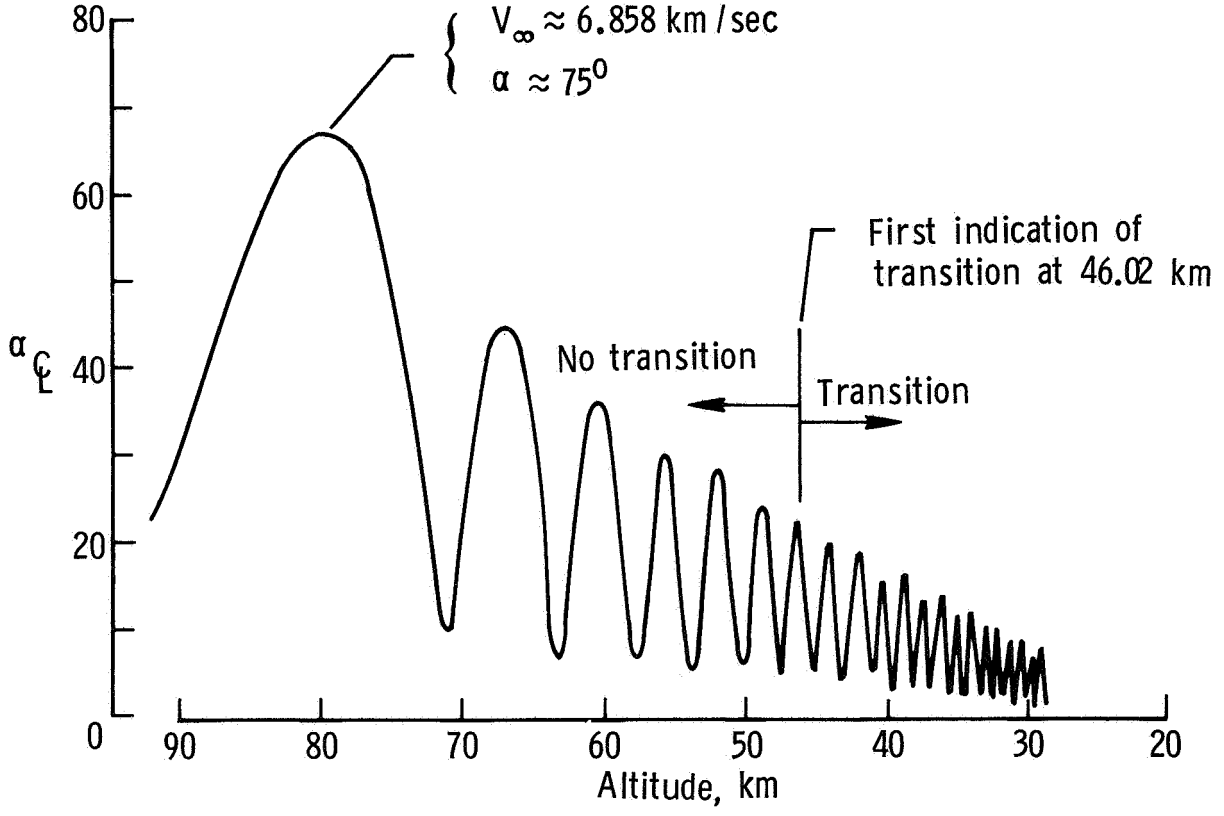

Figure 2.- Cone center-line angle of attack during reentry.

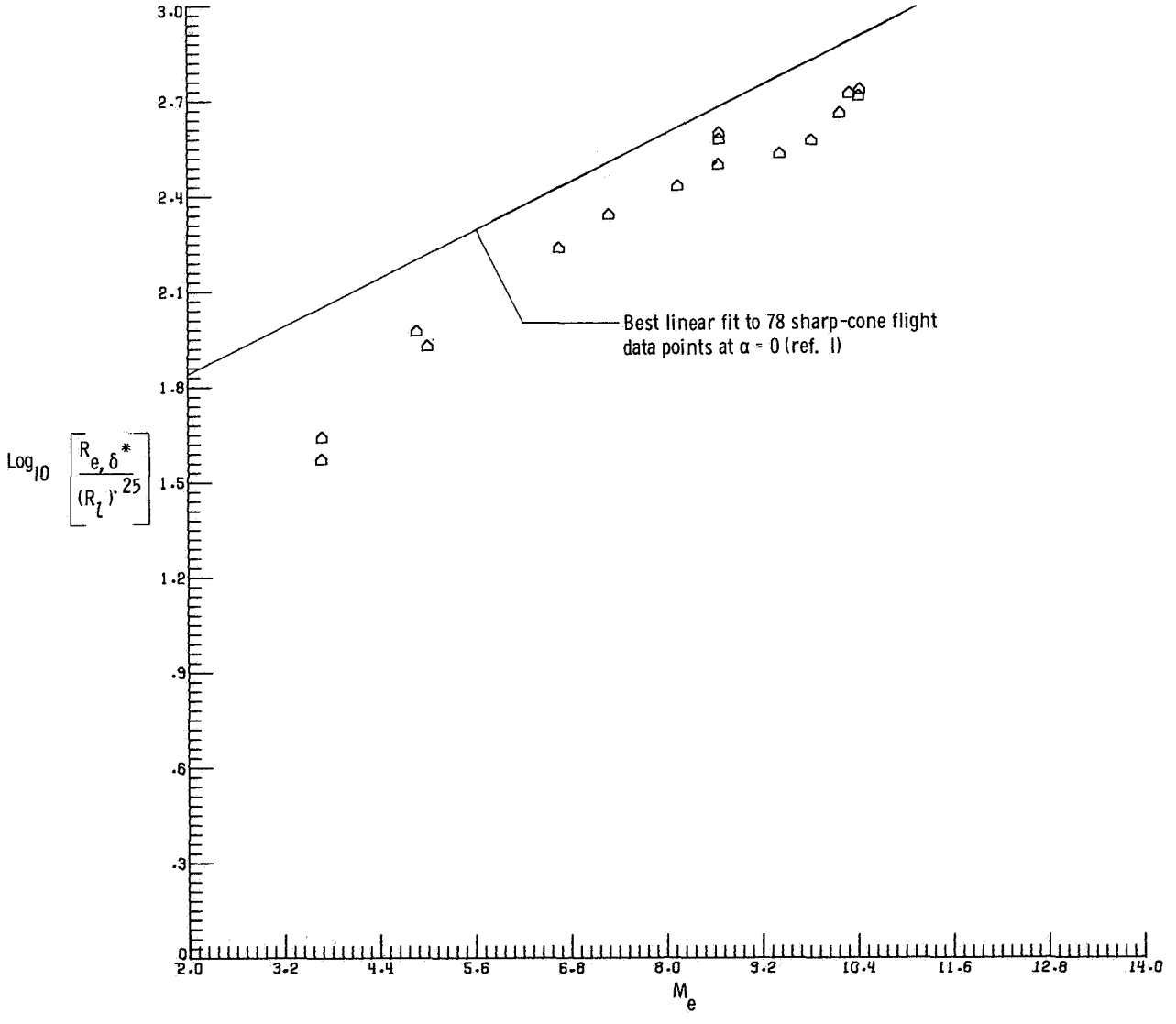

Figure 3.- A correlation of transition flight data from acoustic sensors using local Mach number. ℓ = 1 m (3.048 ft).

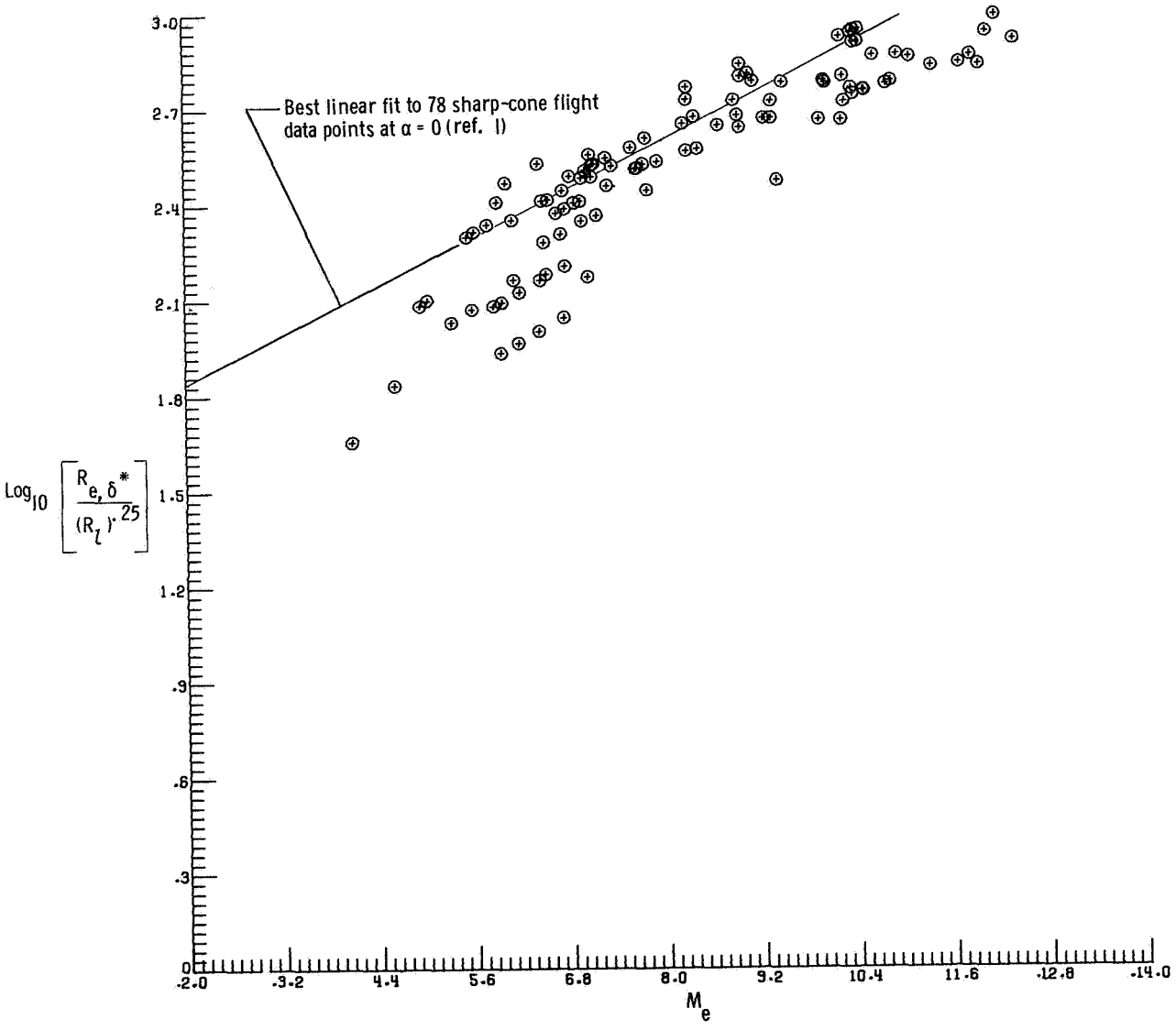

Figure 4.- A correlation of transition flight data from electrostatic sensors using local Mach number. l = 1 m (3.048 ft).

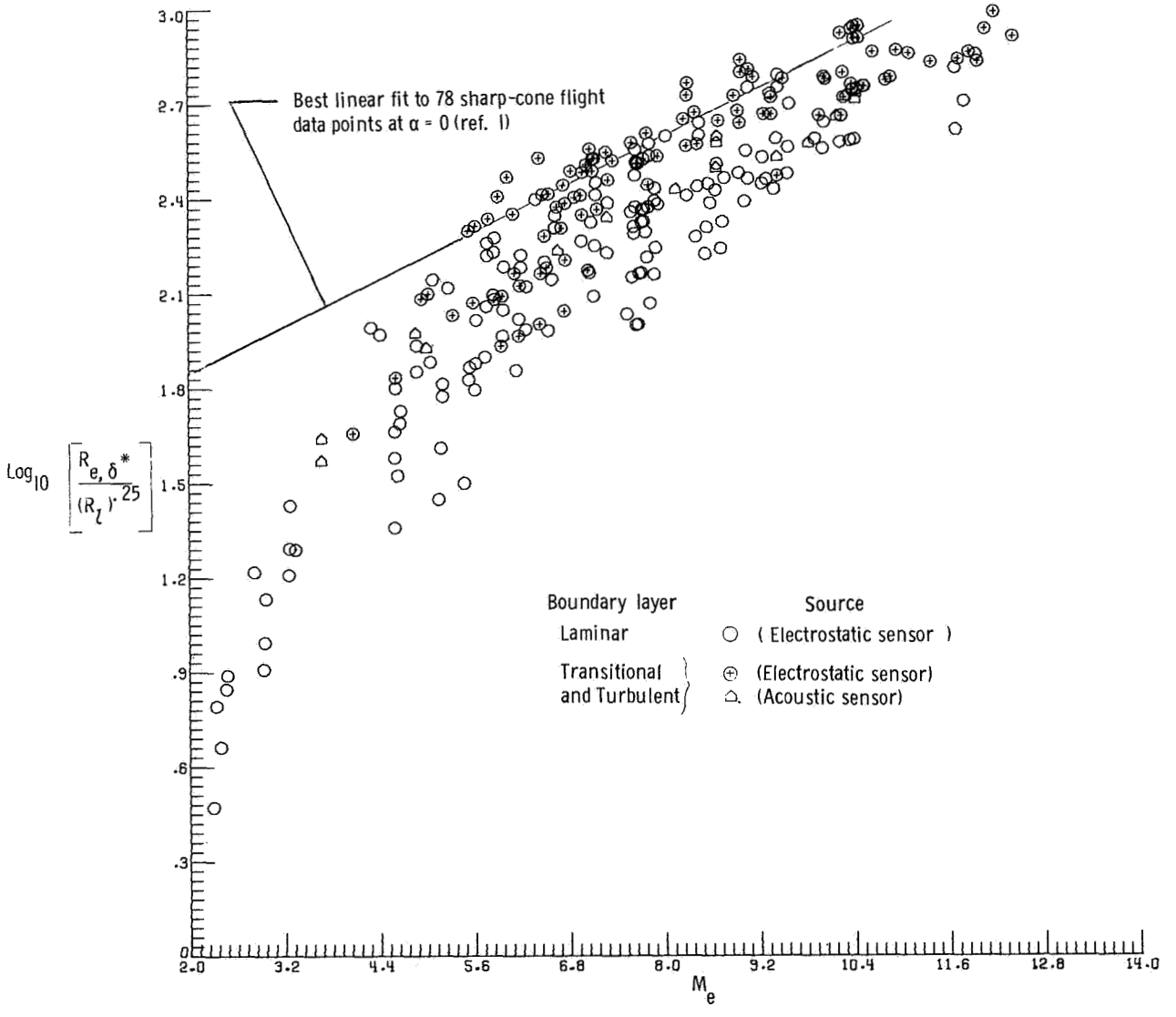

Figure 5.- A correlation of flight data for laminar and turbulent boundary layers from both acoustic and electrostatic sensors using local Mach number. l = 1 m (3.048 ft).

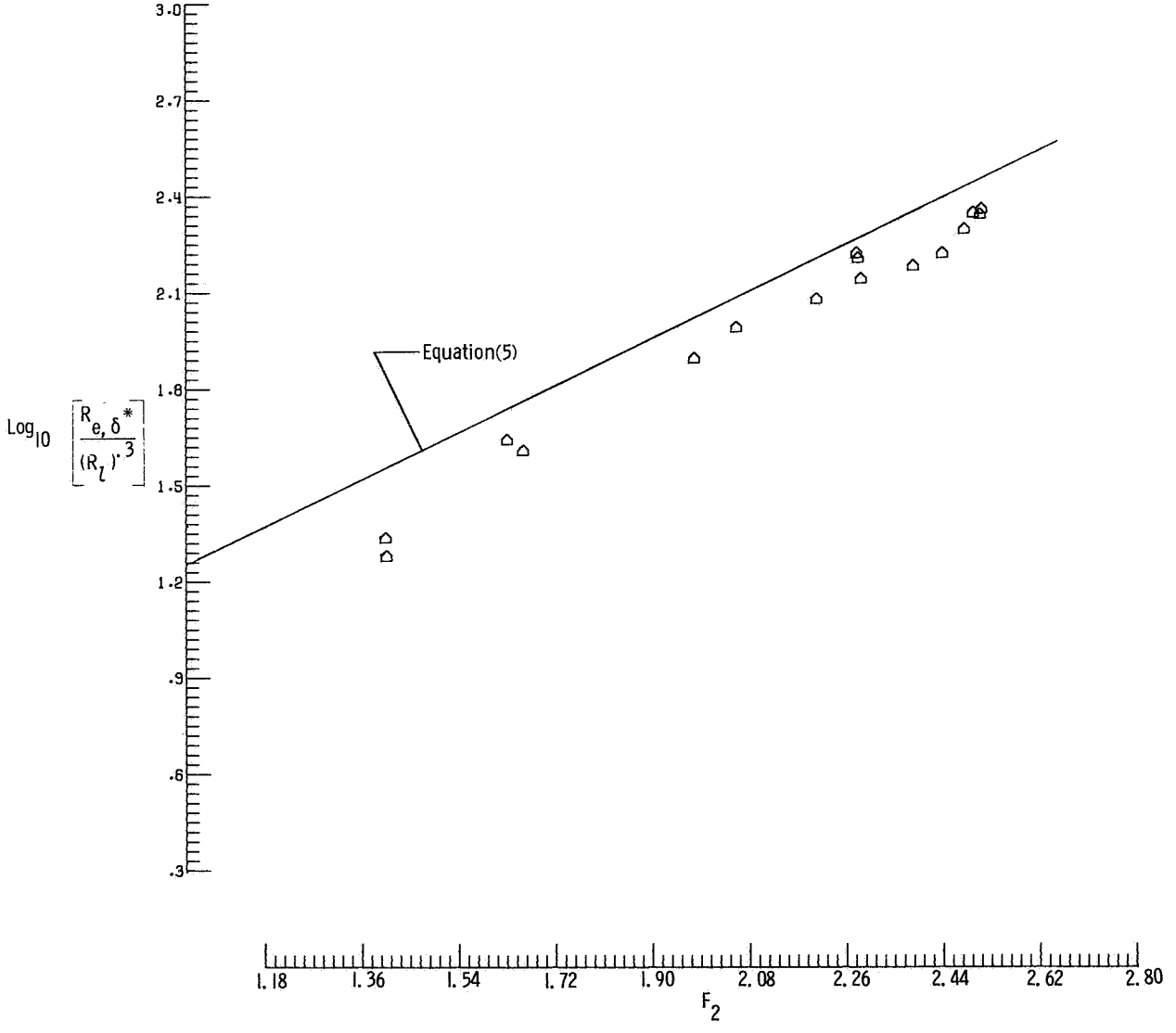

Figure 6.- A statistical correlation of transition flight data from acoustic sensors. l = 1 m (3.048 ft).

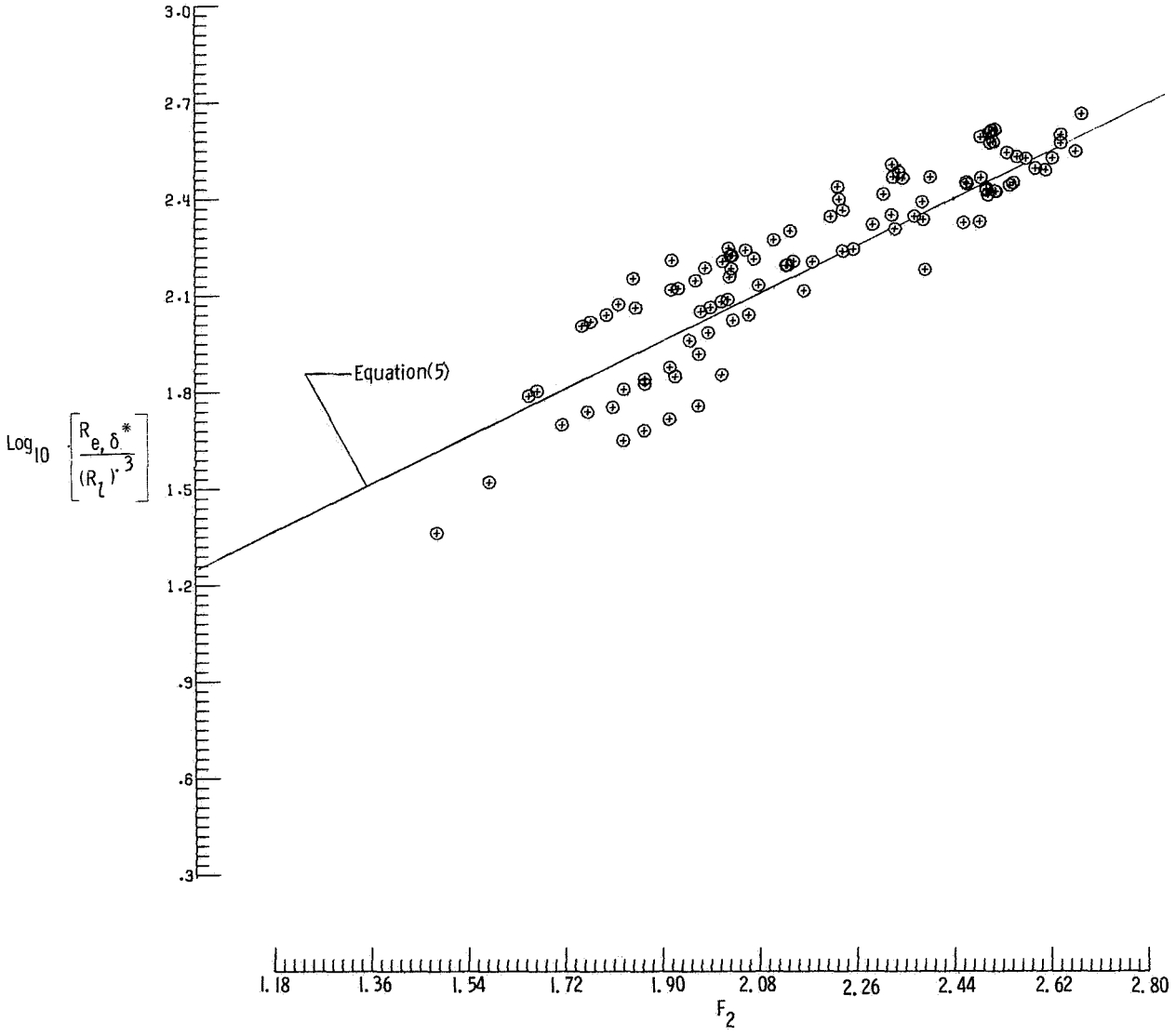

Figure 7.- A statistical correlation of transition flight data from electrostatic sensors. l = 1 m (3.048 ft).

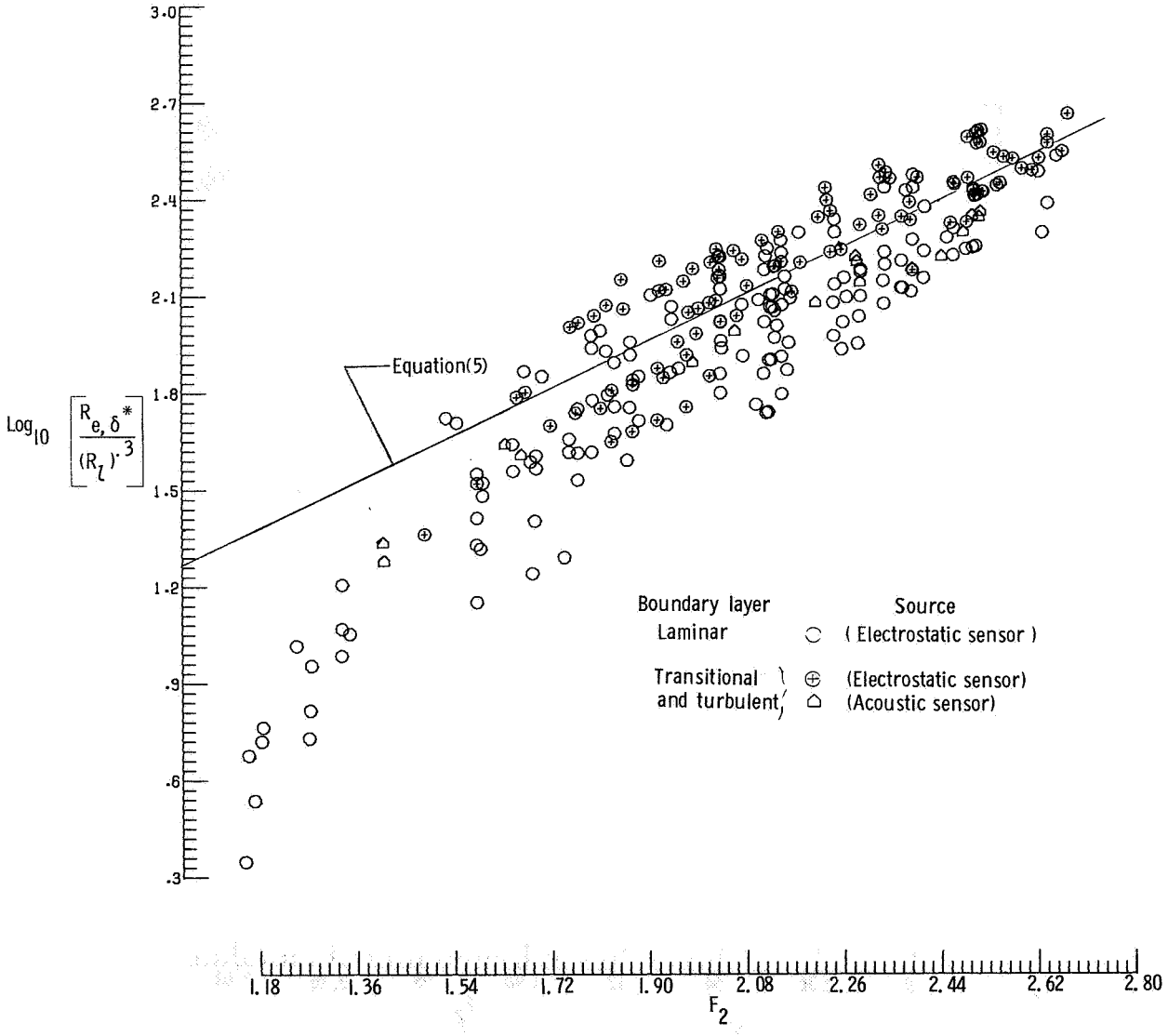

Figure 8.- A statistical correlation of flight data for laminar and turbulent boundary layers from both acoustic and electrostatic sensors. l = 1 m (3.048 ft).

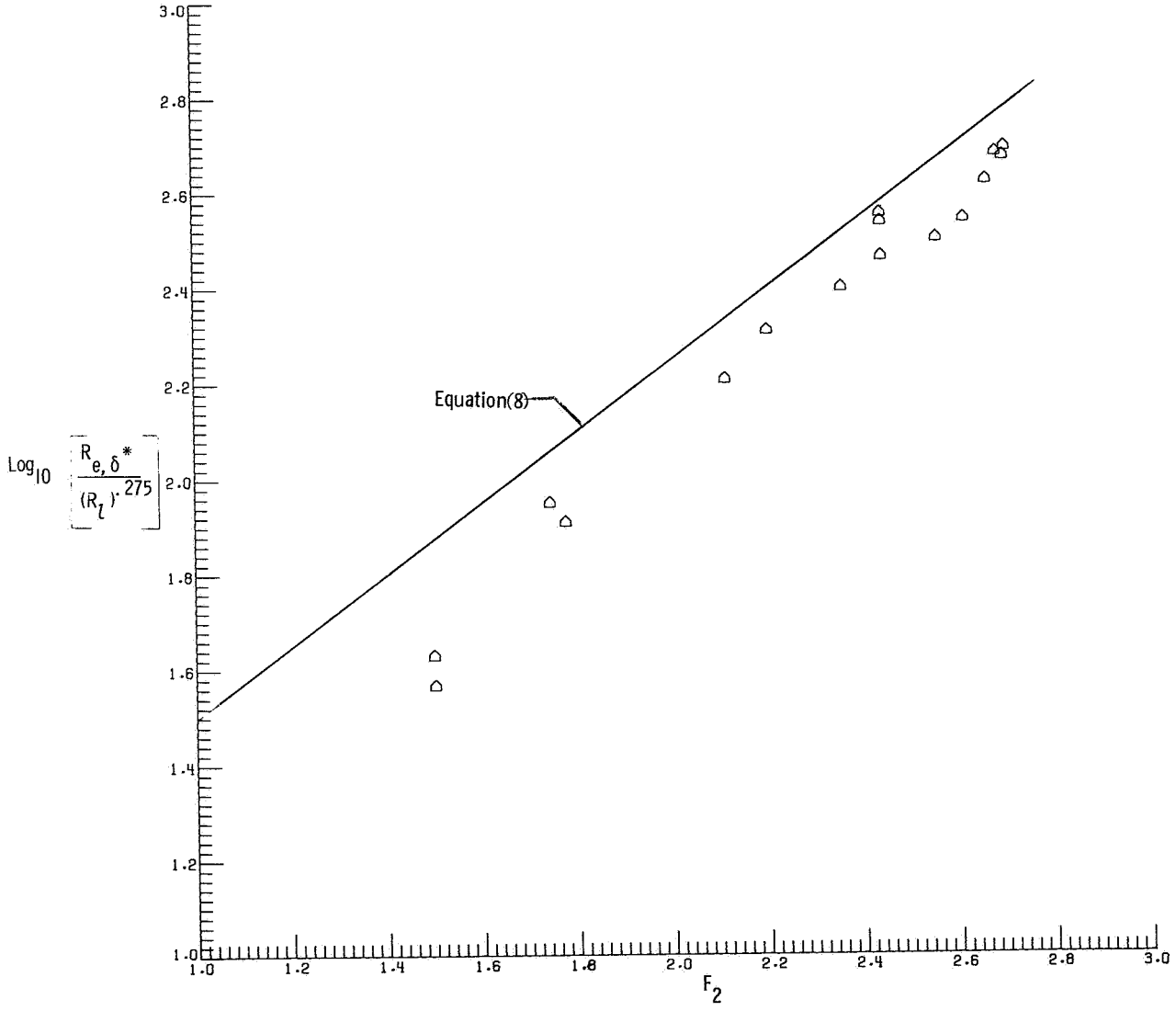

Figure 9.- A statistical correlation of transition flight data from acoustic sensors. l = 0.3048 m (1 ft).

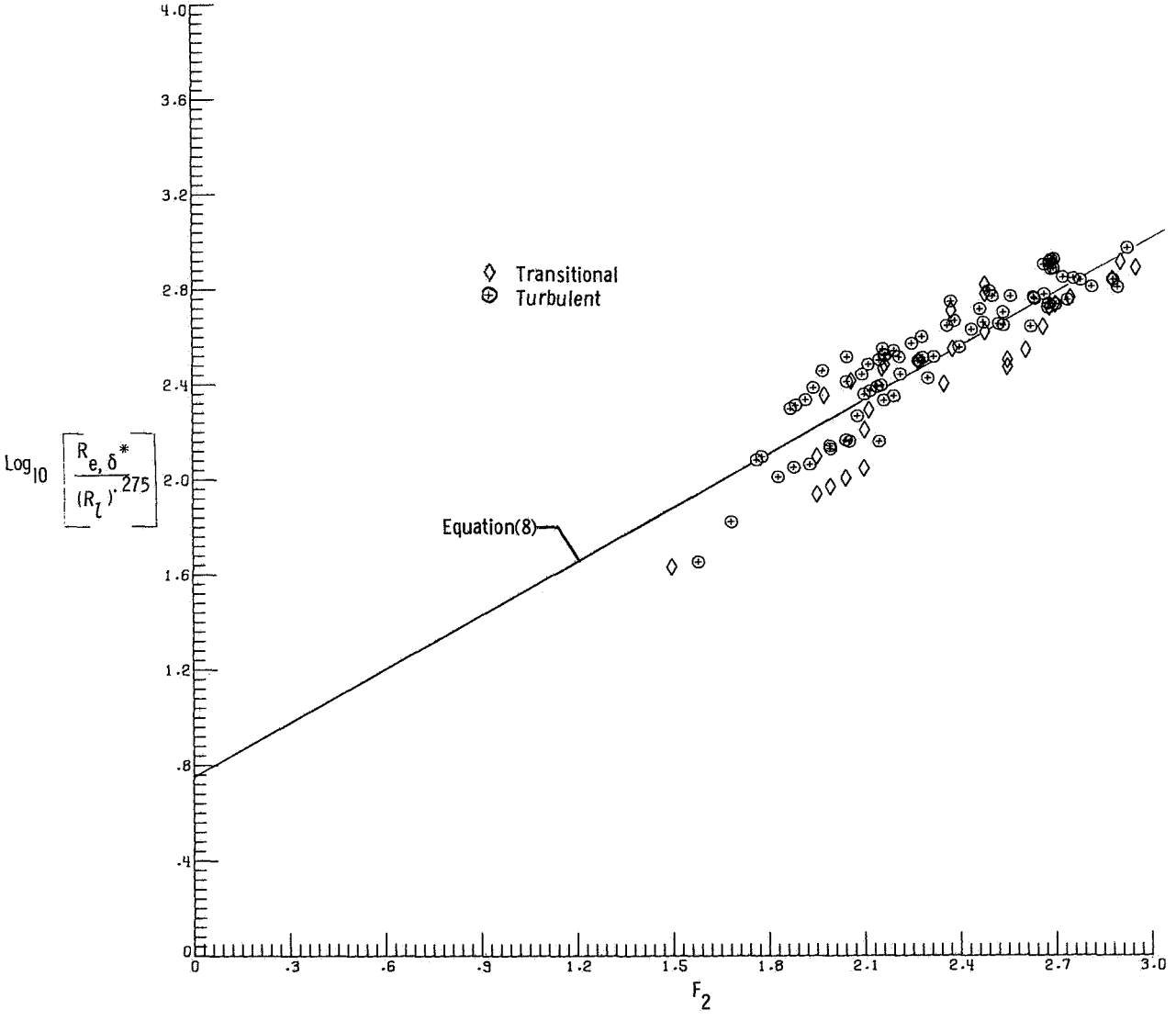

Figure 10.- A statistical correlation of transition flight data from electrostatic sensors. $\ell = 0.3048$ m (1 ft).

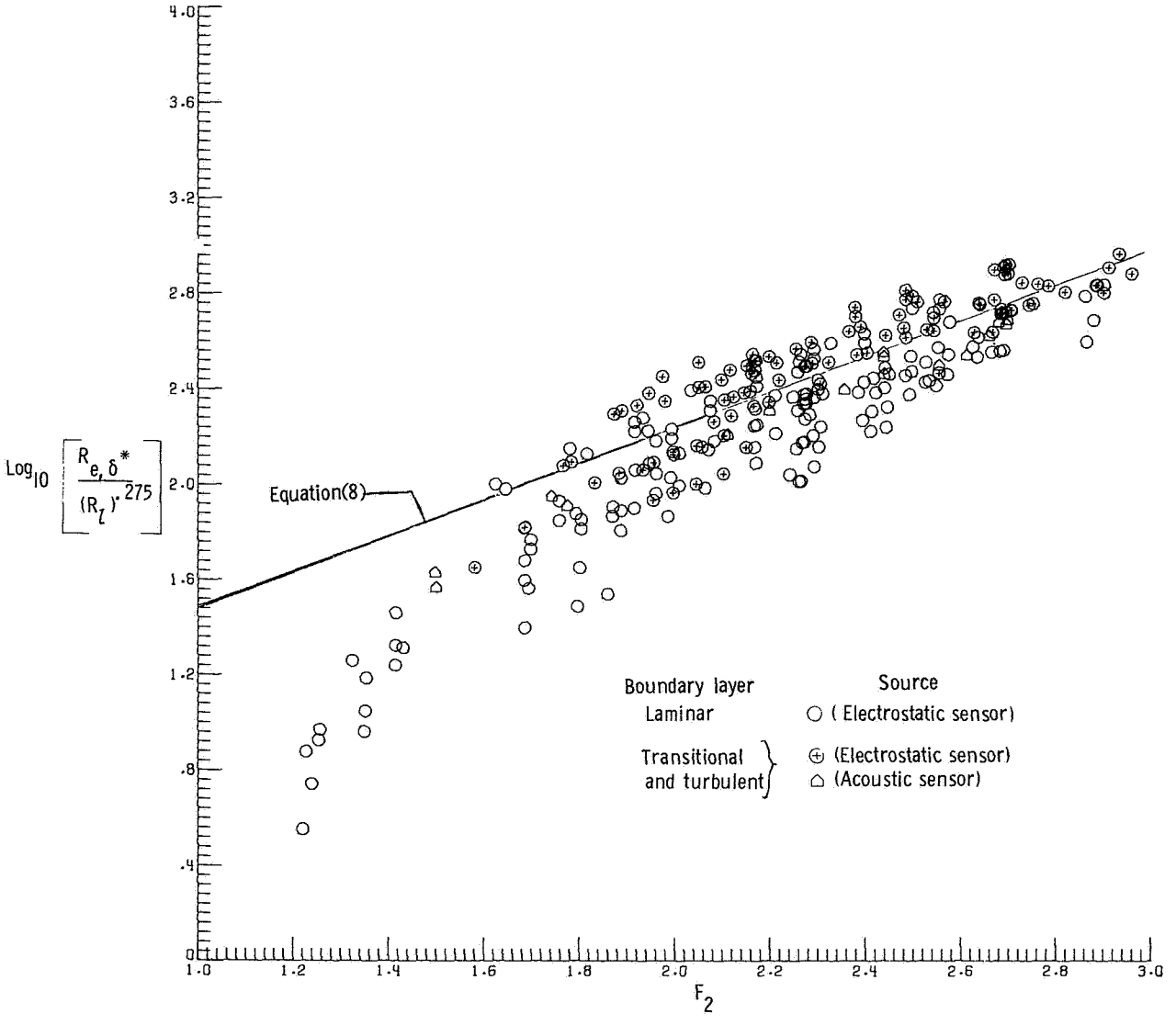

Figure 11.- A statistical correlation of flight data for laminar and turbulent boundary layers from both acoustic and electrostatic sensors. l = 0.3048 m (1 ft).

NATIONAL AERONAUTICS AND SPACE ADMINISTRATION
WASHINGTON, D.C. 20546

OFFICIAL BUSINESS
PENALTY FOR PRIVATE USE $300

SPECIAL FOURTH-CLASS RATE
BOOK

POSTAGE AND FEES PAID
NATIONAL AERONAUTICS AND
SPACE ADMINISTRATION
451

U.S. MAIL

POSTMASTER: If Undeliverable (Section 158
Postal Manual) Do Not Return

"The aeronautical and space activities of the United States shall be conducted so as to contribute . . . to the expansion of human knowledge of phenomena in the atmosphere and space. The Administration shall provide for the widest practicable and appropriate dissemination of information concerning its activities and the results thereof."

—NATIONAL AERONAUTICS AND SPACE ACT OF 1958

NASA SCIENTIFIC AND TECHNICAL PUBLICATIONS

TECHNICAL REPORTS: Scientific and technical information considered important, complete, and a lasting contribution to existing knowledge.

TECHNICAL NOTES: Information less broad in scope but nevertheless of importance as a contribution to existing knowledge.

TECHNICAL MEMORANDUMS: Information receiving limited distribution because of preliminary data, security classification, or other reasons. Also includes conference proceedings with either limited or unlimited distribution.

CONTRACTOR REPORTS: Scientific and technical information generated under a NASA contract or grant and considered an important contribution to existing knowledge.

TECHNICAL TRANSLATIONS: Information published in a foreign language considered to merit NASA distribution in English.

SPECIAL PUBLICATIONS: Information derived from or of value to NASA activities. Publications include final reports of major projects, monographs, data compilations, handbooks, sourcebooks, and special bibliographies.

TECHNOLOGY UTILIZATION PUBLICATIONS: Information on technology used by NASA that may be of particular interest in commercial and other non-aerospace applications. Publications include Tech Briefs, Technology Utilization Reports and Technology Surveys.

Details on the availability of these publications may be obtained from:

SCIENTIFIC AND TECHNICAL INFORMATION OFFICE

NATIONAL AERONAUTICS AND SPACE ADMINISTRATION

Washington, D.C. 20546